

A westerly dominated Early Cretaceous eolian system in the Hami Basin, NW China

Dehai Zhang^{1,2}, Guocan Wang^{2,†}, Alex Pullen³, Jordan T. Abell^{4,5}, Feng Cheng^{1,6,†}, Tianyi Shen², Junliang Ji⁷, and Meng Zhang⁸

- ¹Key Laboratory of Orogenic Belts and Crustal Evolution, Ministry of Education, School of Earth and Space Sciences, Peking University, Beijing 100871, China
- ²Center for Global Tectonics, Hubei Key Laboratory of Critical Zone Evolution, School of Earth Sciences, China University of Geosciences, Wuhan 430074, China
- ³Department of Environment Engineering and Earth Sciences, Clemson University, Clemson, South Carolina 29634, USA
- ⁴Department of Geosciences, University of Arizona, Tucson, Arizona 85721, USA
- ⁵Department of Earth and Environmental Sciences, Lehigh University, Bethlehem, Pennsylvania 18015, USA
- ⁶Yunnan Key Laboratory of Earth System Science, Yunnan University, Kunming 650500, China
- ⁷School of Geography and Information Engineering, China University of Geosciences, Wuhan 430074, China
- ⁸Xinjiang Mineral Resources Research Center, Xinjiang Institute of Ecology and Geography, Chinese Academy of Sciences, Urumqi 830011, China

ABSTRACT

Cretaceous eolian deposits provide evidence of variations in the tropical-subtropical atmospheric circulation under greenhouse conditions. However, the misinterpretation of many such deposits as fluvial or deltaic originally hindered precise paleoclimatic reconstructions. Here we report a newly identified Early Cretaceous desert in the Hami Basin, China, which helps understand spatial-temporal variations in aridity and atmospheric circulations within central East Asia during the Early Cretaceous. The Liushuquan Formation is composed of >300-m-thick eolian deposits interpreted as an intermontane erg environment. Paleocurrent indicators within the straight-crested dunes of the Liushuquan Formation yield a mean trend of 101.3° (± 10.1°, 1 standard deviation) throughout the formation, consistent with near-surface westerly winds. Paleo-atmospheric circulation superimposed on topographic effects led to widespread eolianite accumulation during the Early Cretaceous. Combined with the spatiotemporal changes in desert distributions and prevailing surface wind patterns in East Asia, these observations are consistent with the migration of the subtropical high-

Guocan Wang https://orcid.org/0000-0003

†Guocan Wang, wgcan@cug.edu.cn; Feng Cheng, cfcf.chengfeng@gmail.com

pressure belt during the Early Cretaceous. We propose the following paleo-atmospheric model: (1) During the late Berriasian–Valanginian, the subtropical high belt drifted southward and northward over shorter time scales within the spatial domain of the paleo-Ordos Basin, then shifted southward at least past the Ordos Basin; (2) until the late Hauterivian–Barremian, the subtropical high-pressure zone was primarily located between the northwestern Tarim Basin and the Ordos Basin; and (3) a significant southward shift of the subtropical high-pressure zone occurred during the Aptian–Albian.

INTRODUCTION

Reconstructing atmospheric circulation patterns and their spatiotemporal variations during warm periods is crucial for understanding the dynamics of Earth's climate system under greenhouse conditions (Hasegawa et al., 2012; Cao et al., 2020; Wang et al., 2023). As a paradigm of a historical greenhouse Earth, the late Mesozoic witnessed the aridification and development of deserts over areas much greater than those of modern deserts (Rodríguez-López et al., 2014; Cao et al., 2020). Aridification within the East Asian continental interior in response to the largely Cenozoic growth of the Himalayan Mountain belt and expansion of the Tibetan Plateau is well documented (e.g., Kutzbach et al., 1993; Garzione, 2008; An et al., 2001; Zhang et al., 2007; DeCelles et al., 2007b; Quade et al.,

2011; Xu et al., 2013; Xia et al., 2023). However, the causation, timing, and spatial extent of aridity during the Mesozoic amalgamation of East Asia are less well understood. A shift away from humid depositional environments to more semi-arid and arid environments has been recognized in Upper Jurassic-Lower Cretaceous strata exposed in the East Asian continental interior (Hendrix et al., 1992; Eberth et al., 2001; Vincent and Allen, 2001; Xu et al., 2013; De Pelsmaeker et al., 2018; Jolivet et al., 2017; Morin et al., 2018). Influenced by the increase in paleotemperature during the late Mesozoic greenhouse stage (Qiao et al., 2022), the Late Jurassic-Early Cretaceous deserts were widely distributed in northern China between 25°N and 45°N (Xu et al., 2013, 2019a, 2019b, 2021). Deserts are intimately linked to atmospheric circulation, and spatiotemporal changes in the distribution of deserts and prevailing surface winds are preserved in eolianites (Hasegawa et al., 2012; Qiao et al., 2022). These eolian structures have been used to reconstruct lower-level atmospheric circulation over eastern Asia (e.g., Jiang et al., 2001, 2009; Hasegawa et al., 2010, 2012; Xu et al., 2013; Wu et al., 2018, 2023; Cao et al., 2020; Jiao et al., 2020; Qiao et al., 2022; Wang et al., 2023).

Complex wind-water processes can make it difficult to discriminate between mostly eolian systems and other siliciclastic depositional systems worldwide (Al-Masrahy and Mountney, 2015; Li et al., 2018; Wu et al., 2018; Yu et al., 2020). These complexities lead to the incorrect

GSA Bulletin; published online 28 June 2024 https://doi.org/10.1130/B37436.1.

For permission to copy, contact editing@geosociety.org © 2024 Geological Society of America

interpretation of eolian sedimentary structures as subaqueous, ultimately diminishing the new identification of eolian systems in the geologic records (Rodríguez-López et al., 2014). Recent advances in eolian sedimentology have prompted a reinterpretation of numerous clastic sequences, previously classified as aqueous deposits, to be recognized as eolian in origin: e.g., the Upper Cretaceous Tangbian Formation in the Xinjiang Basin (Wu et al., 2018), the Upper Cretaceous Daijiaping Formation in the eastern Hengyang Basin (Huang et al., 2019), the Upper Cretaceous Honghuatao Formation in the Jianghan Basin (Yu et al., 2020), the Upper Cretaceous Zhengyang Formation in the Jianshi Basin (Yu et al., 2021a), the Upper Cretaceous Dajiaping Formation in the southern Liyou Basin (Yu et al., 2021b), the Lower Cretaceous Mangang Formation in the Simao Basin (Wu et al., 2017), and the Lower Cretaceous Nanxin Formation in the Lanping Basin (Li et al., 2018). Precise dating of pre-Quaternary eolian successions has largely been hampered by lack of datable material (Rodríguez-López et al., 2014; Zheng et al., 2015), and too few reliable age constraints limit the application of eolian records in paleoclimatic reconstructions (Wang et al., 2023). Therefore, the identification of deserts, especially those with well-defined ages, substantially enhances the accuracy and precision of reconstructing atmospheric circulation patterns, overcoming the challenges posed by inadequate records and inaccurate and imprecise age constraints (Wang et al., 2023).

Evidence from the Turpan-Hami Basin, China, points to an environment that was conducive to the deposition of mostly fluvial-lacustrine strata during the Early Cretaceous (Wang et al., 2017). The Lower Cretaceous Shengjinkou Formation contains well-preserved egg and skeleton fossils belonging to the pterosaur Hamipterus tianshanensis (Wang et al., 2014, 2017). A U-Pb zircon age of ca. 135.2 Ma for a tuffaceous bed at the top of the Shengjinkou Formation suggests that the upper Shengjinkou Formation was deposited within the Valanginian (Zheng et al., 2023). Here, we report a newly identified Early Cretaceous eolian succession (named as Liushuquan Formation) beneath the Shengjinkou Formation in the Hami Basin. This represents the earliest recorded eolian activity in the Early Cretaceous. The late Berriasian-early Valanginian Liushauquan Formation refines our understanding of paleoclimatic conditions in East Asia during the Early Cretaceous. The goals of this study are to: (1) describe and interpret the depositional environment of the Early Cretaceous Liushuquan Formation in the Hami Basin, (2) unravel the controlling factors of desertification in this area, and (3) integrate our findings with other eolian

records across East Asia during the Early Cretaceous to reconstruct atmospheric circulation patterns.

GEOLOGICAL SETTING

Jurassic-Cretaceous eolian deposits have been recognized throughout East Asia (Fig. 1A; e.g., Jiang et al., 1999, 2001, 2009; Hasegawa et al., 2009, 2010, 2012; Wu et al., 2017, 2018; Li et al., 2018; Morin et al., 2018; Cao et al., 2020; Yu et al., 2020, 2021a, 2021b; Qiao et al., 2022). These deposits generally mark a transition from humid conditions during the Middle Jurassic to more arid conditions during the Late Jurassic-Early Cretaceous (Hendrix et al., 1992; Eberth et al., 2001; Jolivet et al., 2017; Yi et al., 2019). Paleocurrent indicators in eolianites, their spatial and stratigraphic distributions, and regional geography have been used to reconstruct atmospheric circulation over eastern Asia during the Late Jurassic and Cretaceous (e.g., Jiang et al., 2001; Xu et al., 2019a, 2019b), or more specifically, to reconstruct East Asia's position with respect to synoptic scale atmospheric patterns. Specifically, Qiao et al. (2022) recently attributed fluvial-eolian transitions in the Lower Cretaceous strata of the Ordos Basin to expansion and a poleward shift in the region encompassed by the subtropical high-pressure belt.

The general global rise in ocean and atmospheric temperatures during the Late Jurassic is correlated with the expansion of eolian deposition in East Asia (Qiao et al., 2022). This is recorded in the Upper Jurassic-Lower Cretaceous Santai Formation in the Mengyin Basin (Xu et al., 2019b, 2021), the Tianchihe Formation in the Ningwu-Jingle Basin (Xu et al., 2019a), and the Upper Jurassic Qigu Formation in the Junggar Basin (Morin et al., 2018). Influenced by a greenhouse climate during the Early Cretaceous, the areal distribution of ergs grew markedly in East Asia, forming eolian deposits in the top of the Upper Jurassic-Lower Cretaceous Tuchengzi Formation in the Shangyi and Chaoyang-Beipiao basins (Xu et al., 2013), the Lower Cretaceous Yinjinhuoluo, Luohe, and Luohandong formations in the Ordos Basin (Jiang et al., 2001; Qiao et al., 2022), the Lower Cretaceous Kezilesu Group in the Tarim Basin (Jiang et al., 2009), and the Upper Hekou Group in the Xining-Lanzhou basin (Wu et al., 2011; Wang et al., 2023), ultimately forming a southeast-northwest desert belt between 25°N and 45°N in East Asia (Xu et al., 2013). Wedge structures in the eolian strata of the Luohe Formation indicate the occurrence of Cretaceous permafrost in the plateau desert of the Ordos Basin at subtropical paleolatitudes and 3-4 km paleo-altitude (Rodríguez-López et al., 2022).

The Hami Basin, a subdivided part of the larger Turpan-Hami Basin, is located to the south of the eastern Tianshan and north of the Jurotag mountains (Fig. 1B). The eastern Tianshan includes 4000-5000 m peaks of the Bogda, Barkol, and Karlik mountains (Fig. 1B). The Tianshan extends 2500 km, striking approximately northeast-southwest and encompassing parts of northern Tajikistan, Uzbekistan, Kyrgyzstan, and northern Xinjiang Province in China (Şengör et al., 1993; Windley et al., 2007; Xiao et al., 2013; Chen et al., 2018). The Tianshan formed from the accretion of continental blocks between the Tarim Craton and southern Altaids during the Neoproterozoic to Permian and underwent crustal deformation during the Mesozoic and Cenozoic (Şengör et al., 1993; Windley et al., 2007; Xiao et al., 2013; Chen et al., 2020). Low-temperature thermochronology suggests the eastern Tianshan underwent phases of exhumation during the Mesozoic and Cenozoic (e.g., Wang et al., 2008; Gillespie et al., 2017; Chen et al., 2020; He et al., 2022). Analysis of detrital zircon crystals within the area suggests the northern part of the eastern Tianhshan and the Turpan-Hami Basin developed during the Late Jurassic but were later modified during the Cenozoic through subsequent crustal deformation (Fang et al., 2019; Shen et al., 2020). The tectono-geomorphic expression of the southern portion of the eastern Tianshan may have been largely in place since the Mesozoic but provided relatively little detritus to the Turpan-Hami Basin during the Late Jurassic (Gao et al., 2014; Shen et al., 2020). The Turpan-Hami Basin is currently an underfilled flexural foreland basin, in part, because of hyper-arid conditions (Allen et al., 1993, 1994).

Non-marine Mesozoic-Cenozoic strata cover Precambrian crystal basement and folded Paleozoic rocks in the Turpan-Hami Basin (Allen et al., 1993; Zhu et al., 2005). In the Hami Basin, the Lower Cretaceous stratigraphic unit includes the Liushuquan and Dahaidao (or Shengjinkou) formations from bottom to top (Shen et al., 2020; Zhang et al., 2020a). These formations represent the most widely exposed Mesozoic strata in the basin, previously thought to be part of the Paleogene Bakan Formation (Wang, 2007). The Liushuquan Formation is mainly composed of sandstones with large tabular beds that exhibit eolian cross-bedding, indicative of an erg depositional environment (Zhang et al., 2020a). Well-preserved egg, embryo, and skeleton fossils belonging to the pterosaur Hamipterus tianshanensis were discovered in the Dahaidao Formation, whose lacustrine sedimentary sequence is mainly composed of gray-white sandstones (e.g., Wang et al., 2014, 2017). Analysis of boreholes and outcrops indicates that the Early Cre-

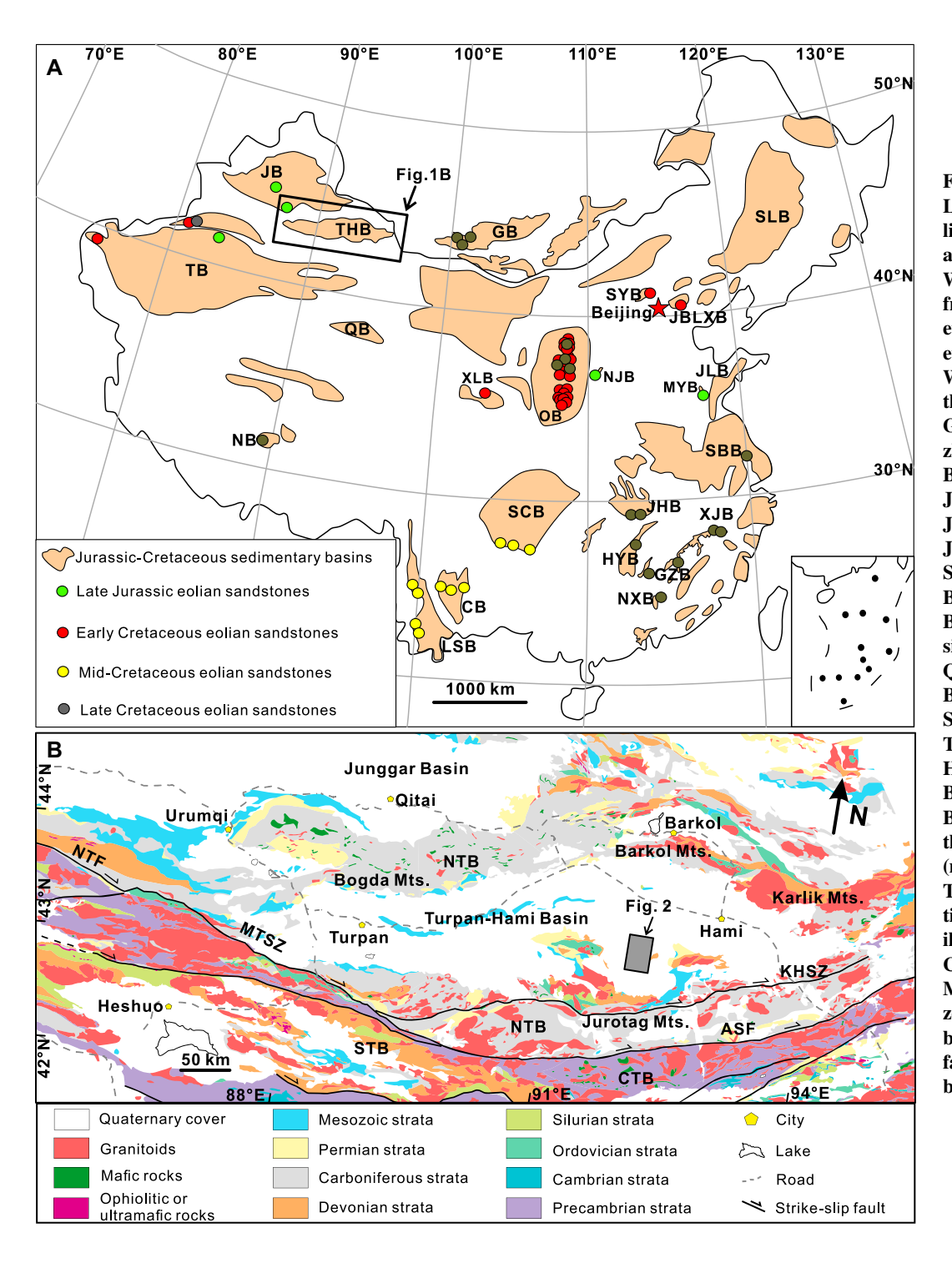


Figure 1. (A) Distribution of the Late Jurassic-Cretaceous eolian sandstones in China and its adjacent areas (modified from Wu et al., 2022; the dataset is from DeCelles et al., 2007a; Xu et al., 2013, 2019a, 2021; Morin et al., 2018; Oiao et al., 2022; Wu et al., 2022, and references therein). CB—Chuxiong Basin; GB-Gobi Basin; GZB-Ganzhou Basin; HYB-Hengyang Basin; JB—Junggar Basin; JBLXB—Jibei-Liaoxi Basin: JHB-Jianghan Basin; JLB-Jiaolai Basin; LSB-Lanping-Simao Basin; MYB-Mengyin Basin: NJB—Ningwu-Jingle Basin; NXB-Nanxiong Basin; OB-Ordos Basin; QB-Qadam Basin; SBB—Subei Basin; SCB—Sichuan Basin; SYB-Shangyi Basin; TB-Tarim Basin; THB-Turpan-Hami Basin; XJB—Xinjiang Basin; XLB-Xining-Lanzhou Basin. (B) Geological map of the eastern Tianshan Orogen (modified after Li et al., 2020). The gray box marks the position of Figure 2. ASF-Aqikekuduke-Shaquanzi fault; CTB—Central Tianshan belt: MTSZ-Main Tianshan shear zone; NTB-North Tianshan belt; NTF-North Tianshan fault; STB-South Tianshan belt.

taceous Liushuquan and Dahaidao formations unconformably overlie Jurassic deposits in the Hami Basin, and Cenozoic strata are unconformable above the Dahaidao Formation (Shen et al., 2020; Zhang et al., 2020a).

MATERIALS AND METHODS

We conducted geologic and stratigraphic investigations in the 4000 km² Hami Basin begin-

ning in 2017 to better understand the Mesozoic–Cenozoic rocks exposed there (Fig. 2). Here, we report on stratigraphic and sedimentological observations of the Liushuquan and Dahaidao formations. The spatial extent of the Lower Cretaceous sedimentary facies was determined by extrapolating observations from outcrop mapping to 16 boreholes in the Hami Basin.

To determine the composition, texture, and diagenetic history of eolian deposits, 15 samples

were collected for petrologic analyses under a polarized microscope in the State Key Laboratory of Geological Processes and Mineral Resources of the China University of Geosciences, Wuhan.

Grain size measurements were made on 33 samples. Samples were selected from eolian dune, interdune, and eolian sheet deposits to determine the grain size characteristics of different facies. Pretreatment of samples prior to analyses included removing organic matter in 10 ml

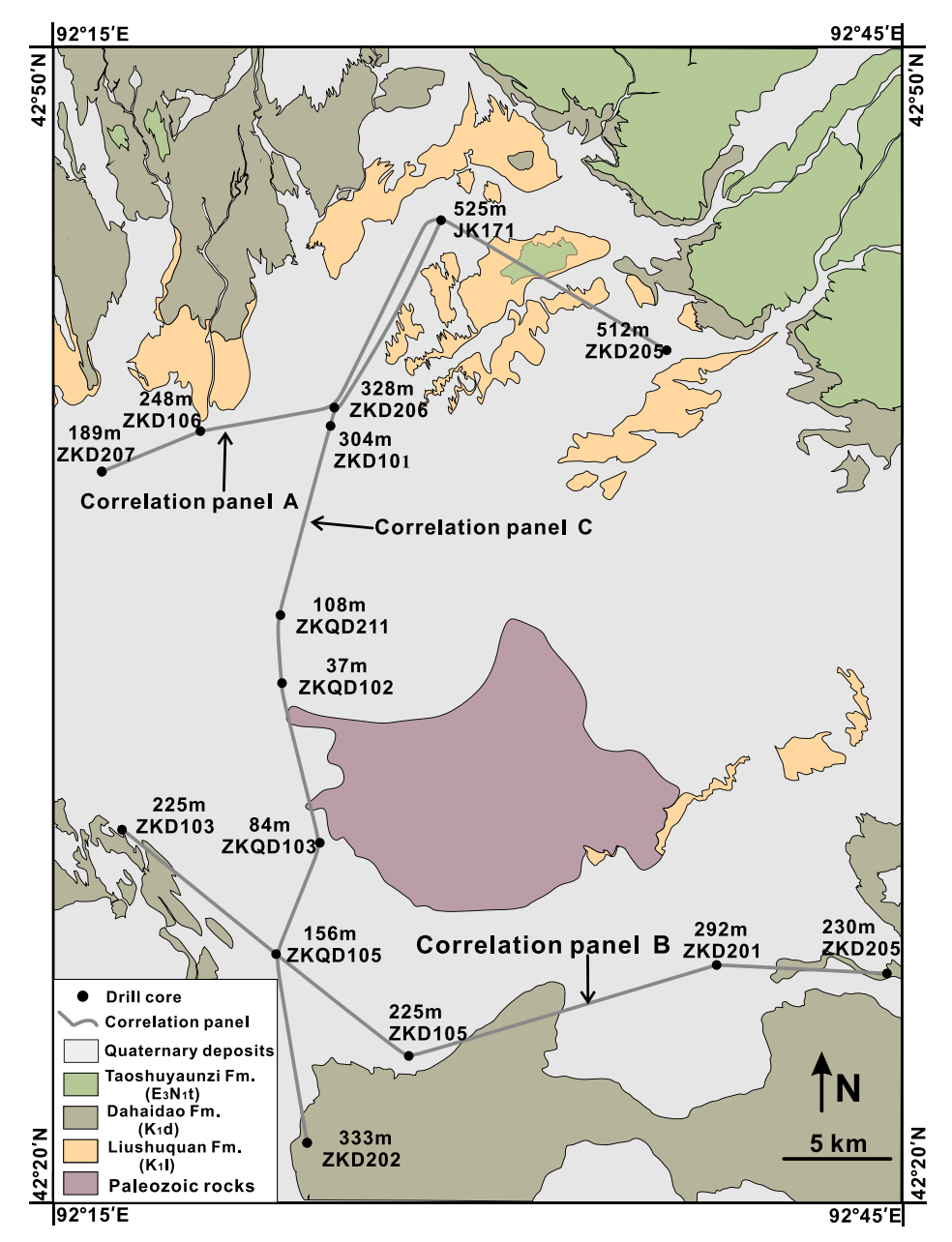


Figure 2. Simplified geological map of the study area in the Hami Basin, China, showing the boreholes and depths. Fm.—Formation.

of 30% $\rm H_2O_2$, removing carbonate with 10 ml of 10% HCl, and dispersing particles with 10 ml of 0.05 mol/l (NaPO₃)₆ in an ultrasonic bath. This pretreatment was aimed at removing the carbonate cement, noting that detrital carbonate clasts were not observed during petrographic analysis. Grain sizes were measured using a Mastersizer 3000 laser particle size analyzer (Malvern Co., Ltd., Malvern, UK) in the Hubei Key Laboratory of Critical Zone Evolution of the China University of Geosciences (Wuhan). The mean grain size, skewness, and kurtosis were calculated following the method of Folk and Ward (1957).

Grain morphometric analysis was done on seven samples from the Liushuquan Formation using a JSM-IT100 scanning electron microscope (SEM) at the Wuhan Sample Solution Analytical Technology Co., Ltd. These samples were pretreated with 20% HCl for 12 h and 20% $\rm H_2O_2$ for 12 h to remove carbonate and organic matter, respectively. Samples were then flushed with distilled water, dried, and finally subjected to a target gold coating in the State Key Laboratory of Geological Processes and Mineral Resources of the China University of Geosciences, Wuhan.

Paleocurrent indicators were measured from the dip azimuths of grain flow strata of straight- and sinuous-crested dunes to reconstruct the paleo-wind direction. Azimuthal data were corrected for a post-Cretaceous vertical axis rotation of 18.6° using the Tarim Basin as a guide because only minor relative movement is thought to have occurred between the Tarim and Turpan-Hami basins since the Cretaceous (Cogné et al., 1995; Hasegawa et al., 2012), without stereographic projection correction due to all measured strata being nearly horizontal (Jiang et al., 2001; Wu et al., 2011).

FACIES ASSOCIATIONS AND INTERPRETATION

Eolian Dune Deposits

Description

This facies association consists of medium- to fine-grained sandstones with well-rounded and high-sphericity grains, organized into planar cross-bedded sets [Sp(e)], trough cross-bedded sets [St(e)], and moderate- to low-angle crossbedded sets [Sl(e)]. The lithofacies Sp(e) are generally organized into 1- to 7-m-thick sets (Fig. 3). The foresets vary from straight to moderately curved, and the dip angle is $\sim 25^{\circ}-30^{\circ}$ near the top of the foresets (Figs. 3A-3C). Sets are internally dominated by grain flow strata comprising centimeter-thick (1-10 cm), tabular or wedge-shaped, massive or inversely graded, medium- to fine-grained sandstones (Figs. 3B-3E). The grain flow strata typically exhibit pin stripe laminations composed of millimeter-thick, fine-grained sandstones (Figs. 3B-3E). The tabular cross-bedded sets are generally arranged as isolated sets, alternating with horizontal to lowangle laminated sandstones [Sh(e)] or lithofacies Sl(e) (Figs. 3F-3H). The bounding surfaces (see "IS" in Figs. 3A, 3D, and 3F-3H) are planar and sub-horizontal and have considerable lateral continuity in the sections parallel to the dip of the cross sets. The dip azimuths (n = 43) of the grain flow strata exhibit a unimodal distribution oriented eastward (Fig. 3I), with a narrow range from 82° to 123° (Table S11). The average value is 101.3° with a standard deviation of 10.1° , and the results of the paleocurrent investigation are presented in Table S1.

The trough cross-bedded sandstones, which exhibit trough-tangential cross-stratification

¹Supplemental Material. Tables S1 and S2 show detailed results of the cross-bedding measurements and grain size analyses, respectively. Please visit https://doi.org/10.1130/GSAB.S.25913866 to access the supplemental material; contact editing@geosociety .org with any questions.

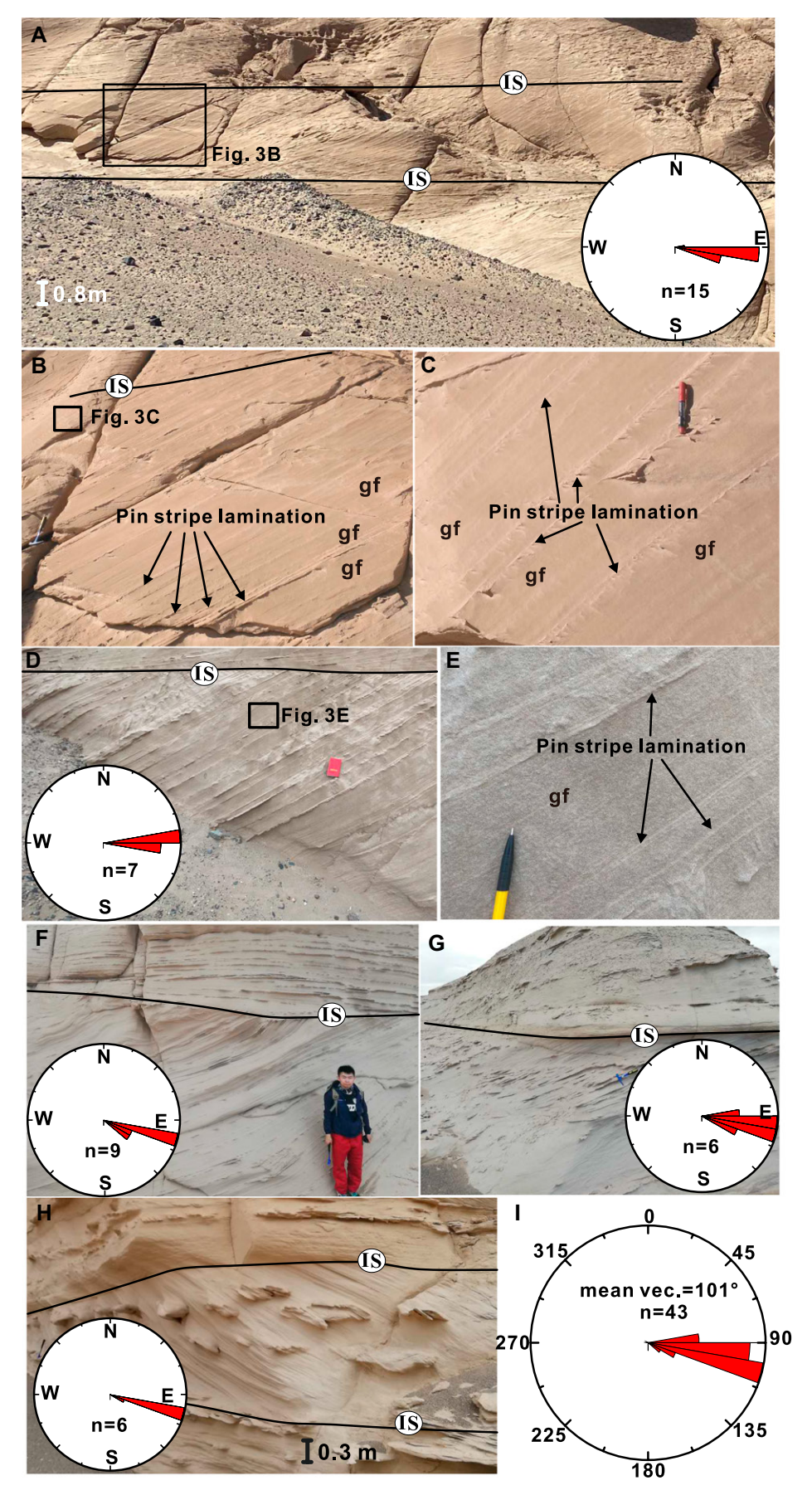


Figure 3. Field photographs and cross-bedding dip directions of planar cross-bedded sandstones, Hami Basin, China. (A) Planar cross-bedded sandstones bounded by planar, sub-horizontal bounding surfaces; (B–E) planar cross-bedded sets composed of grain flow strata and pin stripe laminations; (F–H) planar cross-bedded sandstones overlain by horizontally laminated sandstones; (I) rose diagram indicating the cross-bedded sandstones. IS—interdune surfaces; gf—grain flow strata; n—number of samples; mean vec.—mean vector.

(Figs. 4A-4C), are organized into 0.5- to 6-m-thick sets. From the section perpendicular to the dip direction of the cross-stratifications and bounding surfaces, the cross sets form trough outlines (Figs. 4B and 4C). Foresets are moderately curved, displaying a dip-directional spread up to 50° in a single set (Fig. 4A). The dip direction (n = 73) clusters at 60° – 120° , showing a mean foreset azimuth toward 100° (Fig. 4D). The cross-bedded sets are internally formed by centimeter-thick (1–10 cm), wedge-shaped, inversely graded or non-graded grain flow strata and millimeter-thick pin stripe laminations (Figs. 4E and 4F). The stacked sets of the lithofacies St(e) are separated by low-angle inclined, downwind-dipping bounding surfaces truncating the underlying sets (see "S" in Figs. 4A-4C). In a single set, the cross-bedded sets are truncated by downwind-dipping concave-up surfaces (see "R" in Fig. 4C), whose dip direction is the same as that of the cross-stratifications (see "C" in Fig. 4C). The penecontemporaneous deformation structures (e.g., convolute bedding) are common in the cross-bedded sets (Fig. 4G).

The moderate- to low-angle cross-bedded sandstones are mostly 0.4-4 m thick, extending tens of meters laterally (the maximum outcrop extent; Fig. 5A). These cross-bedded sets exhibit tangential terminations on the bounding surfaces, and the dip angle of the cross-bedded sets increases gradually upward (Fig. 5A). From the section transverse to the dip direction of the cross sets and bounding surfaces, both cross strata and bounding surfaces form trough outlines (meters to tens of meters wide; Fig. 5B). The vertical stacking of these lithofacies SI(e) is overlain by lithofacies St(e) sandstones (Fig. 5C). The stacked sets are separated by low-angle inclined, downwind-dipping bounding surfaces truncating the underlying sets (see "S" in Figs. 5A and 5B). The downwinddipping concave-up bounding surfaces (see "R" in Figs. 5A and 5B) occur within sets of cross strata and are truncated by the low-angle

Geological Society of America Bulletin

inclined bounding surfaces. Cross-bedded sets are internally composed of wind-ripple strata appearing as millimeter-thick, inversely graded, medium- to fine-grained sandstones (Figs. 5D and 5E). The wind-ripple strata normally show pin stripe laminations (Figs. 5D and 5E).

Sandstones of this facies association are mainly composed of quartz (~50%), lithics $(\sim 40\%)$, and feldspar $(\sim 10\%)$, and the cement is calcite and anhydrite (Figs. 6A-6D). In SEM photos, the quartz surfaces are well-rounded (Figs. 6E-6I). Surficial microstructures, such as dish-shaped impact scars, smooth surfaces, and silica precipitation, were observed on the quartz surface (Figs. 6E-6J). The mean grain diameter of sandstone samples from this facies association is 111.9-200.7 µm with a standard deviation of 27.6 μm. The skewness of these samples ranges from -0.16 to 0.61, with an average value of 0.23 and a standard deviation of 0.22. Kurtosis values are between -1.20 and -0.22, with an average of -0.75. The results of the grain size analyses are presented in Table S2. Cumulative particle-size distributions (Visher, 1969) suggest that sandstones consist primarily of saltated (70%-90%) and suspended (10%-30%) particles, without bedload particles, indicating "twosegment style" grain size distributions (Fig. 6K). Grain size distributions show a relatively concentrated major peak between 2 φ and 3 φ with minor distributed peaks (Fig. 6L).

Interpretation

The presence of medium- to fine-grained sandstones with large-scale cross-beddings, comprising grain flow strata, wind-ripple strata, and pin stripe laminations, suggests eolian dune deposits (Kocurek, 1991; Pye and Tsolar, 2009; Li et al., 2018; Xu et al., 2019a; Yu et al., 2020, 2021a, 2021b). Grain flow strata indicate deposition in a well-developed slipface with a flow separation zone (Kocurek, 1991; Rodríguez-López et al., 2008). Pin stripe laminations, which separate the grain flow strata, are formed by the downwind settling of fines in a moving sand avalanche of eolian dunes (Xu et al., 2019a). The presence of grain flow strata and pin stripe laminations suggests that the dunes are oriented with the crestlines transverse to the prevailing paleowind (Kocurek, 1991; Jones et al., 2016; Xu et al., 2019a; Yu et al., 2021a). The unimodal pattern of paleocurrents with low dispersion and the expressive sets of planar cross-stratification indicate that migration of the slightly crescentic dunes with straight crestlines formed the lithofacies Sp(e) (Kocurek, 1991; Wu et al., 2017; Reis et al., 2019; Yu et al., 2020). The mean azimuth of foresets of straight-crested dunes after magnetic deviation correction (82.7°) indicates that the prevailing lower-level winds in the Hami Basin were westerlies. The planar, sub-

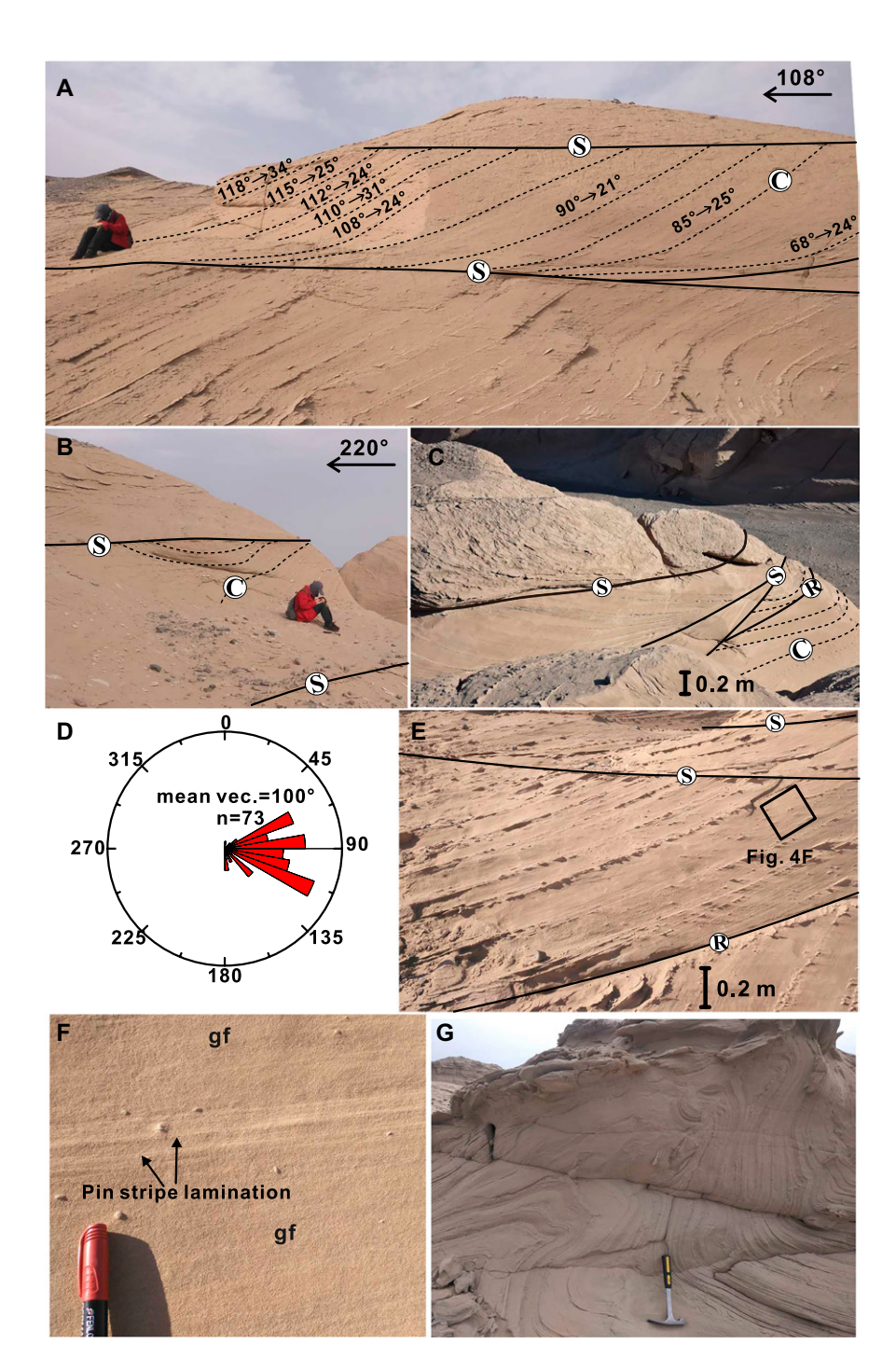


Figure 4. Field photographs and cross-bedding dip directions of trough cross-bedded sandstones, Hami Basin, China. (A) Trough cross-bedded sandstones separated by low-angle inclined, downwind-dipping bounding surfaces; (B) trough outlines of the cross sets from the section perpendicular to the dip direction of the cross-stratifications and bounding surfaces; (C) photograph showing bounding surfaces and cross-bedded sets; (D) rose diagram indicating the cross-bedding dip directions of the trough cross-bedded sandstones; (E, F) trough cross-bedded sandstones composed of grain flow strata and pin stripe laminations; (G) softsediment deformations showing folded lamination and slump lamination. S—superimposition surfaces; C—cross-beddings; R—reactivation surfaces; n—number of samples; mean vec. mean vector; gf—grain flow strata. The numbers before each arrow and after each arrow represent the azimuth of the dip direction and the dip angle of the cross-beddings, respectively.

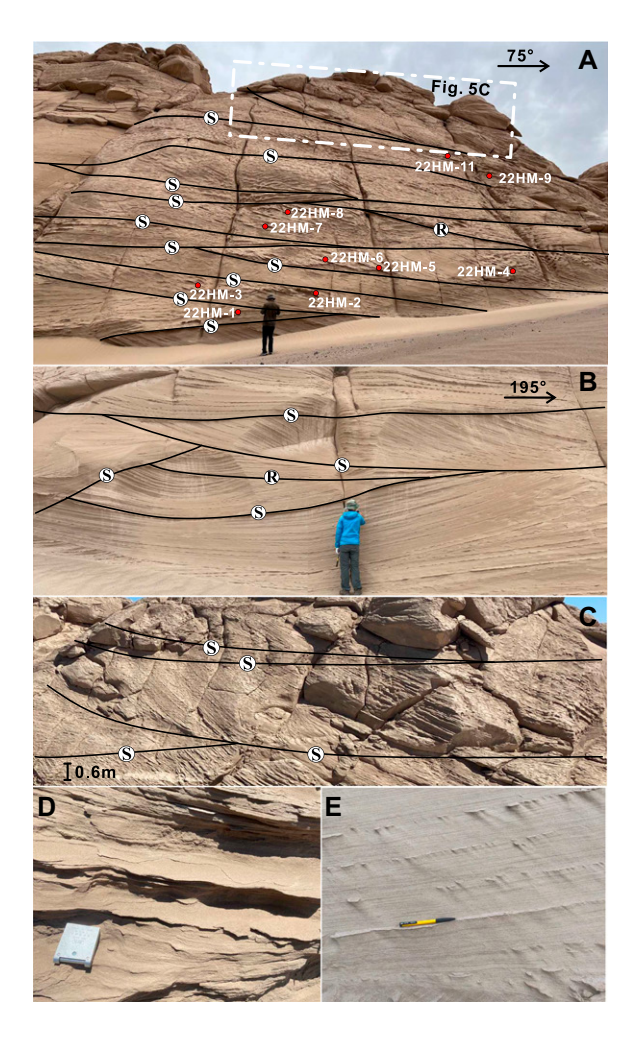


Figure 5. Field photographs of moderate- to low-angle crossbedded sandstones, Hami Basin, China. (A) Moderate- to low-angle cross-bedded sets exhibiting tangential terminations on the bounding surfaces; (B) cross sets and basal bounding surfaces forming trough outlines from the section transverse to the dip direction of the cross sets and bounding surfaces; (C) trough cross-bedded sandstones overlying the vertical stacking of the moderate- to low-angle cross-bedded sandstones; (D, E) wind-ripple strata appearing as millimeter-thick, inversely graded, medium- to fine-grained sandstones. S—superimposition surfaces; **R**—reactivation surfaces.

horizontal surfaces (see "IS" in Figs. 3F–3H) are interpreted as interdune surfaces resulting from the migration and climbing of dunes and interdune areas (Jones et al., 2016).

The trough geometry and high dispersion of paleocurrents suggest that the migration of crescentic dunes with sinuous crestlines formed the lithofacies St(e) (Kocurek, 1991; Jones et al., 2016; Yu et al., 2020, 2021a). The downwind-dipping concave-up surfaces (see "R" in Fig. 4C) are interpreted as reactivation surfaces, which suggest erosion of the lee face of the eolian dune due to changes in the airflow on the lee slope (Kocurek, 1991; Rodríguez-López et al., 2008). The low-angle inclined, downwind-dipping bounding surfaces (see "S" in Figs. 4A and 4C) are interpreted as superimposition surfaces, indicating the migration of crescentic bedforms on the lee slope of the underlying dunes (Rodríguez-López et al., 2008, 2013; Yu et al., 2020). The paleocurrents measured from lithofacies St(e) exhibit trends similar to those of lithofacies Sp(e), indicating a consistent westerly wind direction. The deformation of cross-bedded sets is a common

natural phenomenon in ancient eolian deposits and is usually triggered by animals, rains, or earthquakes (e.g., Rodríguez-López and Wu, 2020).

The wind-ripple strata with moderate- to lowangle dips are interpreted as the result of the accumulation and migration of wind ripples on gentle eolian slopes (Kocurek, 1991, 1996; Jiao et al., 2020). Pin stripe laminations, which separate the wind-ripple strata, form from the downwind settling of fines in wind-ripple troughs (Xu et al., 2019a). The facies association, characterized by a vertical package of moderate- to lowangle wind-ripple strata, a large lateral extent, and a vertical relationship with superimposed trough cross-bedded sandstones, is interpreted as draa plinth deposits (Rodríguez-López et al., 2008). The trough geometry and tangential sets on the low-angle bounding surfaces result from the migration of crescentic bedforms with sinuous crestlines (Scherer et al., 2007; Rodríguez-López et al., 2008). The low-angle inclined, downwind-dipping bounding surfaces, truncating the underlying sets (see "S" in Figs. 5A and 5B), are interpreted as superimposition surfaces

formed by the migration of secondary dunes on the frontal face of large-scale bedforms lacking well-developed slipfaces (Scherer et al., 2007; Rodríguez-López et al., 2008; Yu et al., 2021b). The downwind-dipping concave-up bounding surfaces (see "R" in Figs. 5A and 5B) are likely reactivation surfaces, formed due to reworking during periods with varying wind directions (Yu et al., 2020).

Surficial microstructures on the quartz grains, including the dish-shaped impact scars, smooth surfaces, and silica precipitation, originate from direct impacts during eolian transport and abrasion, as well as from eolian weathering and dissolution in arid environments (e.g., Wu et al., 2017; Li et al., 2018; Cao et al., 2020; Yu et al., 2020). The eolian dune sandstones exhibit a pronounced positive grain size skew, as compared to the beach sand's negative bias (Friedman, 1961, 1967; Li et al., 2018). The relatively concentrated distribution between 2ϕ and 3ϕ indicates that the grains of sandstones have been wellsorted by wind-driven processes (Rodríguez-López et al., 2006), which are characteristic of both modern and ancient desert deposits (e.g., Qian et al., 2011; Wu et al., 2017, 2018; Li et al., 2018; Jiao et al., 2020).

Eolian Interdune Deposits

Description

This facies association can be divided into two types: type 1 and type 2. Type 1 consists of medium- to fine-grained sandstones [lithofacies Sh(e)] organized into sets 0.3-3.5 m thick and extending laterally for tens of meters. The lenticular unit ends laterally by pinching out between lithofacies St(e) (Fig. 7A). The tabular unit is interbedded with tabular cross-bedded sandstones and wet interdune deposits (see discussion of type 2 in this paragraph) and is bounded by flat and sub-horizontal interdune surfaces (see "IS" in Figs. 3F-3H and 7B). These sandstones are organized into low-angle to horizontal, millimeter-spaced, parallel laminations exhibiting pin stripe lamination and inverse grading (Figs. 7C and 7D). The pin stripe laminations are fine-grained sandstones arranged in millimeter-thick laminae (Figs. 7C and 7D). Ripple marks are visible on the exposed bedding surfaces and indicate coarser-grained crests and finer-grained troughs (Fig. 7E). The wavelength to wave height ratios are mostly >20. Type 2 mainly consists of lenticular mudstone (Fm) and wavy laminated siltstone and fine-grained sandstones (Fw; Figs. 7F-7I). The mudstone consists of meter- to centimeter-thick beds interbedded with eolian sandstones (Figs. 7G-7I). Desiccation crack structures are commonly observed in mudstone with well-sorted sand

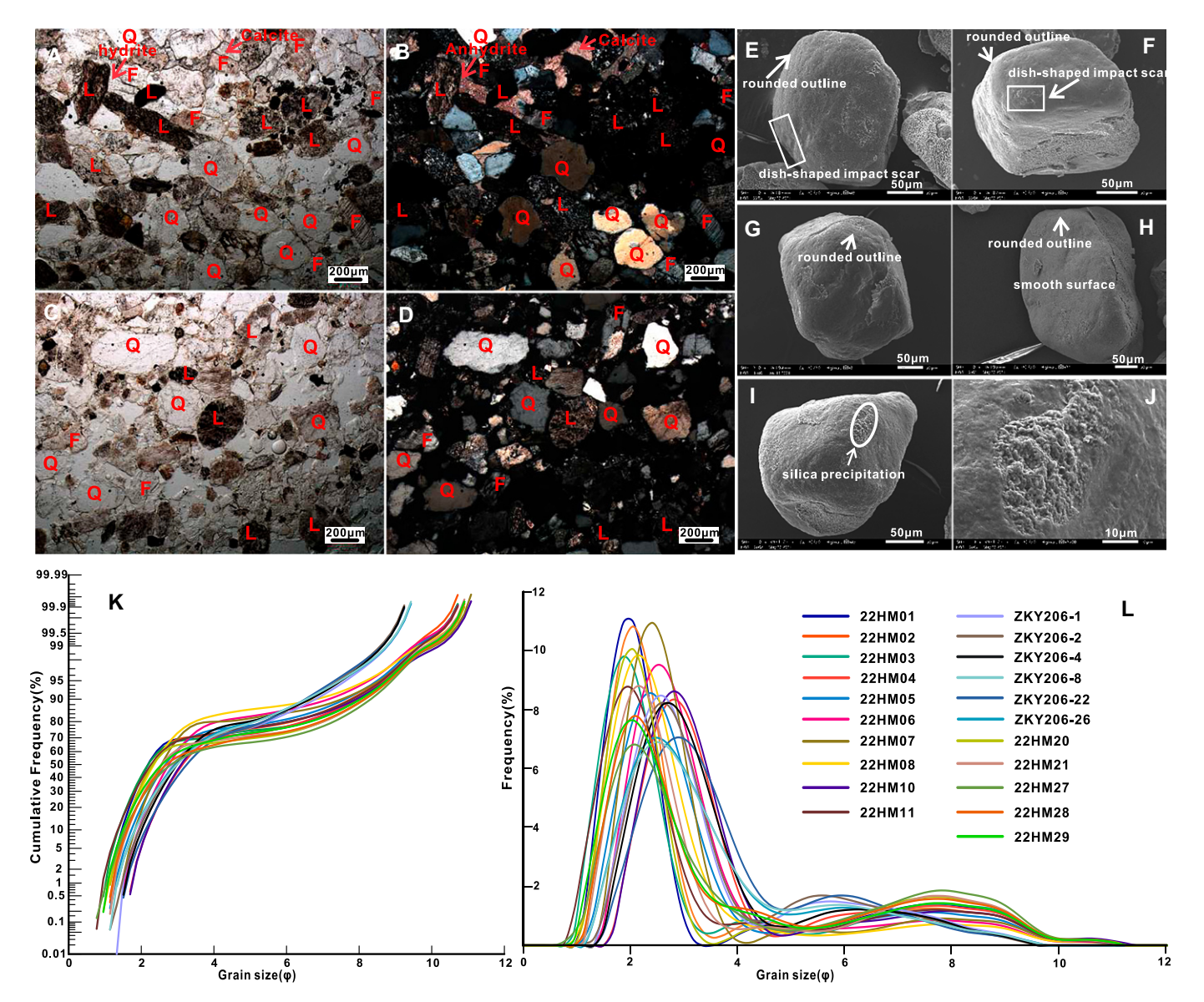


Figure 6. Microscopic features of the eolian dune deposits, Hami Basin, China. (A–D) Representative thin section photos of the eolian dunes deposits. (E–J) Scanning electron microscope images of the quartz grain surface. (K) Grain size cumulative frequency and (L) frequency curves of eolian dune deposits. Q—quartz; F—feldspar; L—lithics.

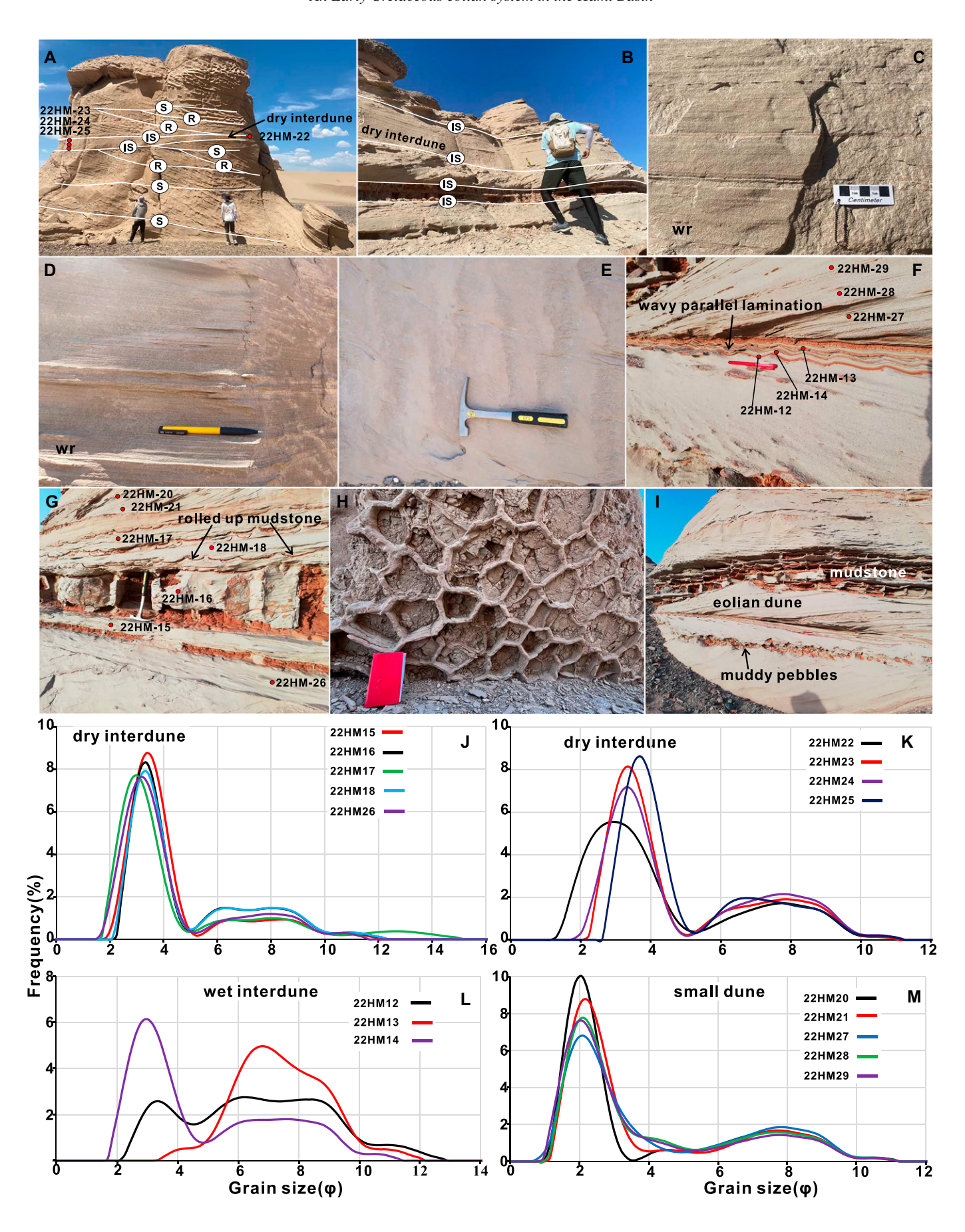
fills (Figs. 7G and 7J), and the thin mudstone is often curved concave up (Fig. 7G). Polygonal sand casts are well preserved on the bottom of overlying eolian sandstone (Fig. 7H). Mud pebbles are associated with some eolian sandstones (Fig. 7I). These beds display sharp contacts with the underlying eolian cross-bedded sandstones and show flat planar contacts with

the overlying eolian beds (Fig. 7I). The grain size distribution curves show that the red wavy laminations are composed of siltstone, while the white wavy laminations consist of fine-grained sandstones (Fig. 7L). The interdune deposits have finer particles than eolian dune deposits, with slightly bimodal grain size distributions (Figs. 7J and 7M).

Interpretation

The horizontal to low-angle, parallel laminations with inverse grading are interpreted as subcritically climbing translatent strata produced by migration and climbing of wind ripples on dry depositional surfaces (Hunter, 1977; Xu et al., 2019a; Yu et al., 2021a). The presence of tabular intervals or lenticular bodies composed of sub-

Figure 7. Field photographs and grain size frequency curves of interdune deposits, Hami Basin, China. (A) The lenticular dry interdune deposits pinching out between cross-bedded sandstones; (B) the tabular geometry bounded by flat and sub-horizontal interdune surfaces; (C, D) close view of dry interdune deposits composed of wind-ripple strata; (E) ripple marks on the exposed bedding surfaces; (F) the wavy sub-parallel siltstones and fine-grained sandstones in the wet interdune deposits; (G) mudstone and desiccation cracks of the wet interdune deposits; (H) polygonal sand mold preserved on the bottom of overlying eolian sandstone; (I) wet interdune deposits showing a sharp contact with the underlying eolian cross-bedded sandstones and a flat contact with the overlying eolian dune; (J–M) grain size frequency curves of interdune deposits. IS—interdune surfaces; S—superimposition surfaces; R—reactivation surfaces; wr—wind-ripple strata.



Geological Society of America Bulletin

critically climbing translatent strata interbedded with cross-bedded sandstones suggests that type 1 represents dry interdune deposits (Kocurek, 1981; Jones et al., 2016; Jiao et al., 2020). The high ripple index is typical for eolian ripples (Rodríguez-López et al., 2008). The bimodal grain size distribution with a moderate degree of sorting indicates a greater proportion of mud components, which is consistent with the features of the dry interdune sandstones (Wu et al., 2017). The occurrence of mudstone, mud pebbles in association with eolian sandstones, and wavy laminations indicates that type 2 represents wet interdune deposits where the water table was relatively high (e.g., Rodríguez-López et al., 2008; Wu et al., 2017, 2018; Li et al., 2018; Jiao et al., 2020; Ma, 2020). The presence of mudstone and desiccation cracks indicates the presence of water at or near the surface followed by drying (Wu et al., 2017; Ma, 2020; Tang, 2020). When the water table decreased, dunes began to migrate, encasing mudstones and forming muddy pebbles (Rodríguez-López et al., 2008; Wu et al., 2017; Li et al., 2018; Tang, 2020). Mudstone, mud pebbles in association with eolian sandstones, and desiccation cracks have been reported in modern and ancient desert environments (e.g., Williams, 2015; Wu et al., 2017; Li et al., 2018; Ma, 2020; Tang, 2020). The wavy lamination formed as a sequence of a high phreatic level causing the adhesion of sand grains to the damp surface (Rodríguez-López et al., 2008; Li et al., 2018; Jiao et al., 2020; Yu et al., 2020, 2021b).

Alluvial Fan Deposits

Description

This facies association can be divided into two types, type 1 and type 2, which are noted in the base portion of the Dahaidao and Liushuaugan formations, respectively. Type 1 is mainly composed of conglomerate lithofacies (Gt, Gcd, and Gh) and pebbly sandstone lithofacies (Sph and Spm; Fig. 8; Table 1). The trough crossstratified conglomerate (Gt) contains cobbleto pebble-sized clasts with coarse to medium sandstone matrix. This lithofacies is crudely to distinctly trough cross-stratified and consists of lenticular geometry up to 1.5 m thick and 5 m wide (Fig. 8B). The lower surface of the lenticular unit is erosional (Fig. 8B). The clastsupported conglomerate (Gcd) comprises cobble- to pebble-sized clasts that are poorly organized and weakly imbricated. Tabular beds are generally ungraded, extend laterally for more than tens of meters, and alternate with pebbly sandstones to form fining upward sequences (Fig. 8D). Locally, thick beds are crudely stratified and commonly include sandstone lenses

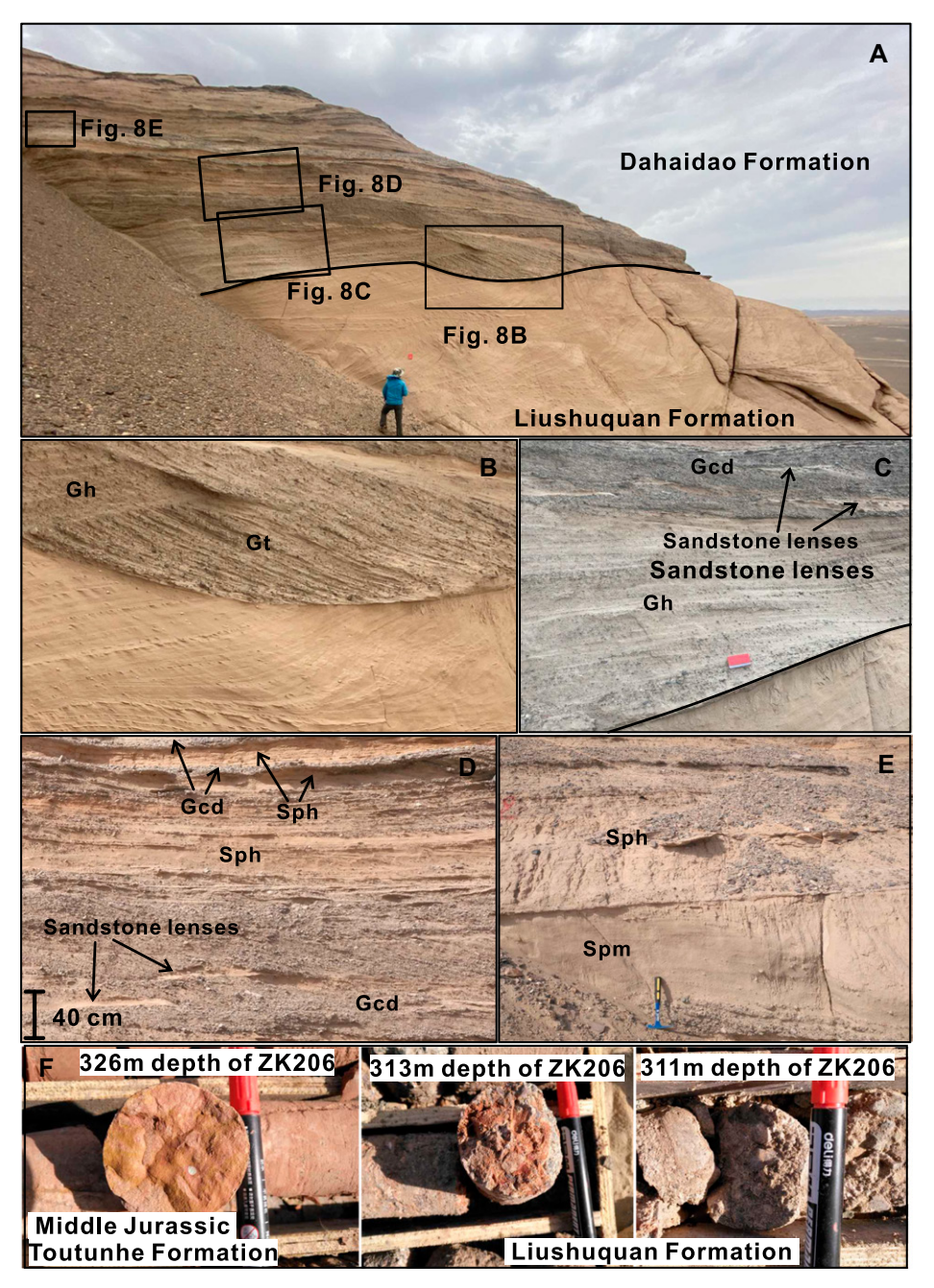


Figure 8. Field photographs of alluvial fan deposits, Hami Basin, China. (A) Alluvial fan deposits at the base portion of the Dahaidao Formation; (B) trough cross-stratified conglomerate (Gt) showing lenticular geometry; (C) parallel-stratified conglomerates (Gh) displaying obvious parallel stratification; (D) clast-supported conglomerates (Gcd) and pebbly sandstones (Sph) showing fining-upward trend; (E) pebbly sandstones being crudely to distinctly stratified (Sph) or partly crudely stratified (Spm); (F) massive matrix-supported conglomerate (Gmm) at the base portion of the Liushuquan Formation.

(Figs. 8C and 8D). The parallel-stratified conglomerate (Gh) consists of pebble-sized clasts within a moderately to well-sorted, sand-sized matrix that is distinctly stratified (Fig. 8C). The matrix displays obvious parallel stratification, and the clasts are generally protruding and oriented parallel to the bedding plane

(Fig. 8C). The pebbly sandstones are coarse- to fine-grained and include pebble-sized gravels, with individual beds typically 0.2–1 m thick. The pebbly sandstones are crudely to distinctly stratified (Sph) or partly crudely stratified (Spm; Fig. 8E). Type 2, identified in the basal portion of the Liushuquan Formation, is dominantly

TABLE 1. DESCRIPTIONS AND INTERPRETATIONS OF LITHOFACIES TYPES OBSERVED IN THE LIUSHUQUAN AND DAHAIDAO FORMATIONS, NW CHINA

| Lithofacies | Description | Interpretation |
|--|--|--|
| Sp(e): planar cross-bedded sandstone | Medium- to fine-grained sandstone; well-sorted; planar cross-bedded sets (1–7 m thick) formed by centimeter-thick (1–10 cm), tabular or wedge-shaped, massive or inversely graded grainflow strata and millimetric pin stripe laminations | Migration of straight-crested eolian dunes (Kocurek, 1991; Reis et al., 2019; Xu et al., 2019a) |
| St(e): trough cross-bedded sandstone | Medium- to fine-grained sandstone; well-sorted; trough cross-bedded sets (0.5–6 m) formed by centimeter-thick (1–10 cm), massive or inversely graded grainflow strata and millimetric pin stripe laminations | Migration of sinuous-crested eolian dunes (Kocurek, 1991; Jones et al., 2016; Reis et al., 2019; Xu et al., 2019a) |
| SI(e): moderate- to low-angle cross-bedded sandstone Sh(e): horizontal to low-angle laminated sandstone | Medium- to fine-grained sandstone; well-sorted; moderate- to low-angle cross-bedded sets formed by millimetric inversely graded laminae Medium- to fine-grained sandstone; well-sorted; horizontal to low-angle laminations formed by millimetric inversely graded laminae | Translatent subcritical wind-ripple migration on dry depositional surfaces (Reis et al., 2019; Xu et al., 2021) Translatent subcritical wind-ripple migration on dry depositional surfaces (Reis et al., 2019; Xu et al., 2021) |
| Fw(e): wavy laminated sandstone and siltstone Gmm: massive matrix- | Fine-grained sandstone and siltstone; moderately to well-sorted; wavy laminations Cobble- to pebble-sized, angular to subangular clasts; poorly sorted | Adhesion of sand grains to the wet surface (Reis et al., 2019; Yu et al., 2021b) Deposits of debris flows (Miall, 2006) |
| supported conglomerate Gcd: clast-supported conglomerate | matrix of sand, silt, and mud; tens of meters thick Cobble- to pebble-sized clasts; coarse to fine sandstone matrix; poorly organized and weakly imbricated gravels; sandstone lenses; tabular | Deposits of gravel sheets emplaced by high-magnitude flood flows (Jo et al., 1997; Hadlari et al., 2006) |
| Gt: trough cross-bedded conglomerate | geometry; commonly overlain by pebbly sandstones Cobble- to pebble-sized clasts; coarse to medium sandstone matrix organized into trough cross-stratifications; lenticular geometry with | Filling of minor channels, scours, and channel pools (Jo et al., 1997) |
| Gh: parallel-stratified conglomerate Gm: mud-clast conglomerate | erosional base Pebble-sized clasts; moderately to well-sorted, sand-sized matrix; distinctly parallel-stratified Granule- to pebble-sized, angular mud clasts; coarse to medium | Deposits of deeper, channelized flow or strong channelized flood (Nemec and Steel, 1984) Rapid deposition from high-energy events within a lacustrine |
| Spm: massive pebbly sandstone | sandstone matrix; abundant pterosaur fossils Coarse- to fine-grained sandstone includes pebble-sized gravels; partly crudely stratified | setting (Wang et al., 2017; Wang, 2019) Rapid deposition from heavily sand-laden flows during waning floods (Jo et al., 1997) |
| Sph: horizontally stratified pebbly sandstone | Coarse- to fine-grained sandstone includes pebble-grade gravels; poorly to moderately sorted; crudely to distinctly stratified | Planar bed flow sédimentation (Jo et al., 1997; Hadlari et al., 2006) |
| Spt: trough cross-bedded pebbly sandstone FI: horizontally laminated | Coarse- to medium-grained sandstone includes mud clasts; distinctly trough-stratified; erosional base Fine- to very fine-grained sandstone; well-sorted; horizontal laminations; | Migration of three-dimensional dunes (Hadlari et al., 2006) Settling of suspended load in standing water (Yu et al., 2021a) |
| sandstone Fm: mudstone | lateral extension for thousands of meters Massive or laminated mudstone | Settling of suspended load in standing water (Yu et al., 2021a) |

composed of massive matrix-supported conglomerates (Gmm). The cobble- to pebble-sized clasts are angular to subangular and supported by a poorly sorted matrix of sand, silt, and mud (Fig. 8F). The massive beds, which are tens of meters thick, unconformably overlie the Middle Jurassic Toutunhe Formation (Fig. 8F).

Interpretation

The lenticular trough cross-stratified conglomerate (Gt) is interpreted as the deposits filling trough-shaped channels after intervals of incision between flood events (Hadlari et al., 2006; Rodríguez-López et al., 2012; Yu et al., 2021a). The clast-supported conglomerate (Gcd) suggests deposits of gravel sheets emplaced by high-magnitude flood flows (Jo et al., 1997; Hadlari et al., 2006; Yu et al., 2021a). The parallel-stratified conglomerate (Gh) implies deeper, channelized flow or strong channelized flood in an alluvial fan (Nemec and Steel, 1984). The pebbly sandstones were deposited on gravel sheets by the waning flood flows (Jo et al., 1997; Yu et al., 2021a). The massive pebbly sandstone (Spm) suggests deposits of direct fallout sedimentation, and the horizontally laminated pebbly sandstone (Sph) is likely the result of upper plane bed sedimentation (Todd, 1989; Jo et al., 1997; Yu et al., 2021a). The overall characteristics of type 1 are consistent with those of streamflow deposits that are similar to those of gravel-bed streams in alluvial fans (Jo et al.,

1997; Hadlari et al., 2006; Yu et al., 2021a). The massive matrix-supported conglomerate at the base of the Liushuquan Formation is interpreted as resulting from the process of high-strength debris flows, representing the most distinctive components of alluvial fan environments (Miall, 2006).

Lacustrine Deposits

Description

This facies association, present in the middle and upper parts of the Dahaidao Formation, is characterized by horizontally laminated sandstone (Fl), mudstone (Fm), and mud-clast conglomerate (Gm). The horizontally laminated sandstone, ranging from fine-grained to very fine-grained (Wang, 2019), is composed of millimeter-thick horizontal laminations (Figs. 9A and 9B). These tabular beds extend laterally for thousands of meters (the maximum outcrop extent). Decimeter- to centimeter-thick mudstone is interbedded within the laminated sandstone (Fig. 9B). Mud-clast conglomerate consists of granule- to pebble-sized, angular clasts of mudstone within a coarse to medium sandstone matrix (Fig. 9C). Pterosaur fossils (bones) are preserved within these coarse clastic layers (Fig. 9D), corresponding to the sites where Hamipterus tianshanensis has been reported (Wang et al., 2017). Desiccation cracks occur within the thin-bedded mudstone in the upper part (Wang, 2019). Locally, coarse- to medium-grained sandstone is present within horizontally laminated fine- to very fine-grained sandstones, appearing as 0.1–0.5 m trough cross sets (Figs. 9E and 9F; Wang et al., 2017). The trough cross-bedded sandstone, which includes mud clasts, incises into underlying deposits, displaying an erosional base (Figs. 9E and 9F; Wang et al., 2017).

Interpretation

The horizontally laminated fine-grained to very fine-grained sandstone and the mudstone are generally interpreted as resulting from suspension deposition in a quiet-water environment (Hadlari et al., 2006; Miall, 2006; Scherer et al., 2007, 2015; Reis et al., 2019). The published grain size results of the fine- to very fine-grained sandstones indicate a shallow lake environment (Wang, 2019). The significant lateral continuity of the horizontally laminated fine-grained to very fine-grained sandstone suggests that deposition occurred in a large, shallow lake basin (Scherer et al., 2015; Wang et al., 2023). Angular mud clasts are interpreted as rip-up clasts, suggesting rapid deposition and short transport distances (Wang et al., 2017). The assemblage of rip-up clasts and pterosaur fossils implies that high-energy events such as storms have rapidly transported these elements within the lake (Wang et al., 2017; Wang, 2019). The presence of desiccation cracks indicates subaerial expo-

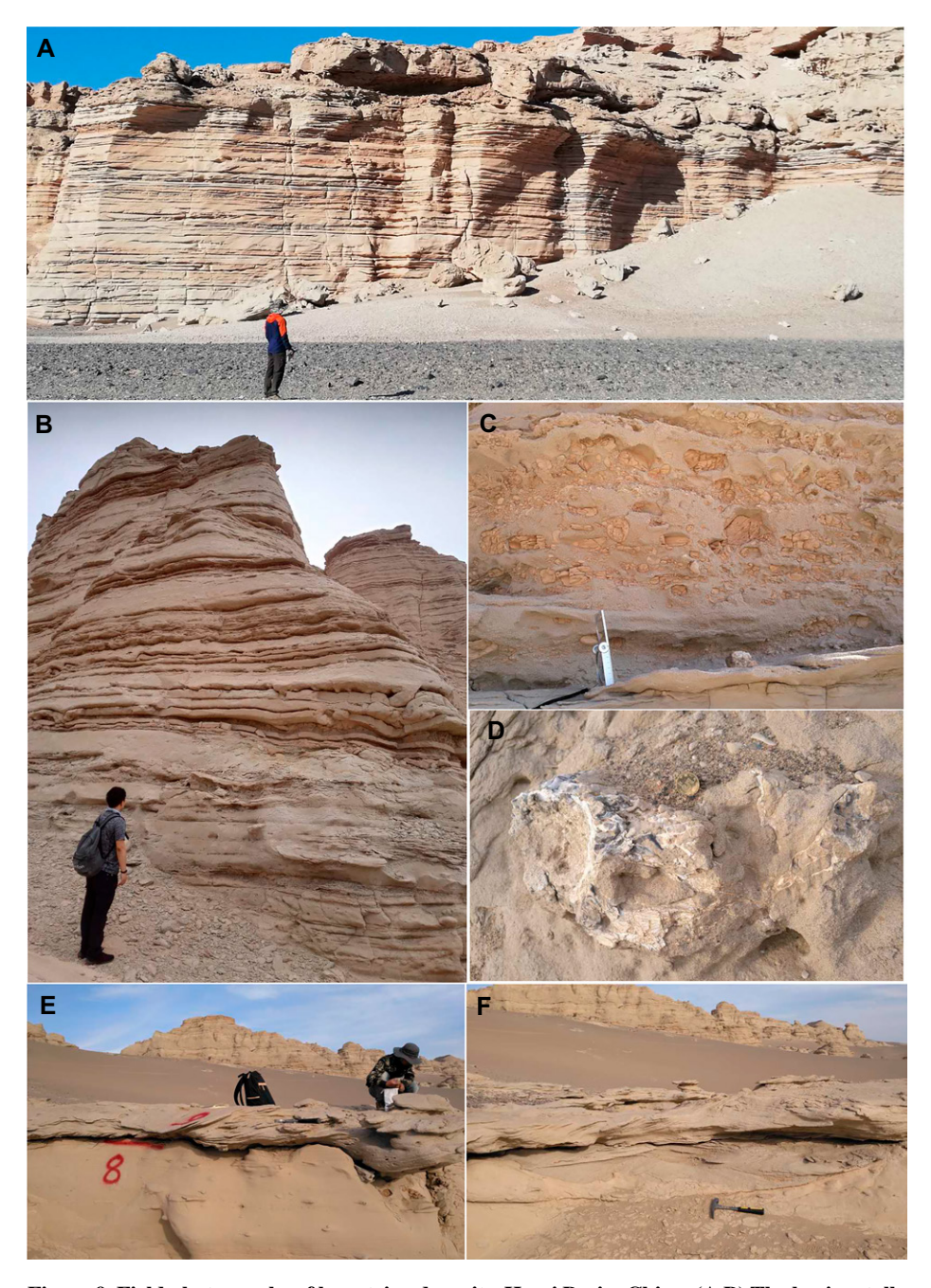


Figure 9. Field photographs of lacustrine deposits, Hami Basin, China. (A B) The horizontally laminated fine- to very fine-grained sandstone (Fl) and mudstone (Fm) in the middle and upper parts of the Dahaidao Formation; (C) mud-clast conglomerate (Gm) composed of angular mud clasts within a sandy matrix; (D) pterosaur fossils (bones) preserved within coarse clastic layers; (E,F) trough cross-bedded pebbly sandstone (Spt) incising into underlying deposits.

sure and a decrease in water level (Wang, 2019). Trough cross-bedded sandstone that incises into underlying laminated sandstones is interpreted as channel deposits (Hadlari et al., 2006). The presence of these channel deposits within the facies association suggests seasonal discharge in a distributary channel within a lake environment (Hadlari et al., 2006).

DISCUSSION

Atmospheric Factors Controlling Early Cretaceous Erg Formation in the Hami Basin

Complex wind-water processes can lead to difficulty in discriminating between mostly eolian systems and other siliciclastic depositional systems (e.g., Rodríguez-López et al., 2010, 2012; Williams, 2015; Wu et al., 2018; do Amarante et al., 2019; Yu et al., 2020). Our investigations suggest, based on sedimentary structures, grain sorting and morphology, grain surface textures, and sedimentary architecture, that the Liushuquan Formation represents a typical erg (Rodríguez-López et al., 2014).

The development of the world's desert deposits is dependent on wind regime, climate, basin area, and the nature of the source rocks (Brookfield and Silvestro, 2010). A multitude of low-temperature thermochronology and detrital zircon chronology studies indicate that the eastern Tianshan was largely shaped during the Late Jurassic and the Turpan-Hami Basin evolved into an intermountain basin located within the eastern Tianshan (e.g., Tang et al., 2015; Gillespie et al., 2017; Fang et al., 2019; Shen et al., 2020; Zhang et al., 2020b; He et al., 2022; Qin et al., 2022). The formation of ergs in narrow intermountain basins is complicated by the blockage of wind energy by surrounding mountains, limiting eolian sand transport (Cao et al., 2020; Zheng et al., 2024). However, many Late Cretaceous ergs have developed in smaller intermountain basins in South China, including the Xinjing Basin (Wu et al., 2018; Cao et al., 2020), Jianshi Basin (Yu et al., 2021a), Jianghan Basin (Yu et al., 2020), Hengyang Basin (Huang et al., 2019), Chaling Basin (Huang et al., 2019), and Jurong Basin (Cao et al., 2023). In addition, many Cretaceous and modern desert areas extended to the high-altitude plateau desert basins with cryospheric processes (Jiao et al., 2020; Wu and Rodríguez-López, 2021; Rodríguez-López et al., 2022). The development of ergs within the intermountain basins and high-altitude plateau desert basins suggests that the winds were not significantly impeded by the surrounding mountains and had sufficient capacity to transport eolian sand into the basins (Cao et al., 2020). In fact, small basins surrounded by high mountains may be windier because of the huge pressure gradients between the mountains and basin floor (Cheng et al., 2015; Zhang et al., 2022). The successive eolian sequences of the Liushuquan Formation, exceeding 300 m, were deposited under the influence of westerlies revealed by the mean azimuth of the foresets of straight-crested eolian dunes.

The sandy desert deposits are the direct result of aridity, but without impeding sediment supply appreciably (Brookfield and Silvestro, 2010; Cao et al., 2020; Wang et al., 2023). Modern and Cretaceous deserts mainly occur under the influence of subtropical latitudes, where air in the equatorial Hadley circulation began to descend, becoming denser and drier (Brookfield and Silvestro, 2010; Hasegawa et al., 2012; Rodríguez-

López et al., 2014; Wu et al., 2018; Yu et al., 2021a). Despite this, many deserts develop in poles and high-altitude plateaus on Earth, where cold and arid conditions prevail (Brookfield and Silvestro, 2010; Wu and Rodríguez-López, 2021; Rodríguez-López et al., 2022). At present, the descending air forms the subtropical high at $\sim 30^{\circ}$ N/S, which controls the geographic distribution of the arid belt on the planet (15°-35°N/ S; Hasegawa et al., 2012; Wang et al., 2023). The Early Cretaceous arid belt produced by the subtropical high in East Asia is wider than its modern counterpart, spanning between 15°N and 45°N (Wang et al., 2023). In spatially adjacent mid-latitude areas, such as the Tarim Basin (paleolatitude $\sim 36.24^{\circ} \text{N} \pm 3.4^{\circ}$) and the Ordos Basin (paleolatitude \sim 36.8°N \pm 4.2°), extensive Early Cretaceous ergs developed at the subtropical paleo-latitude (see Hasegawa et al., 2012, and references therein). Previous paleomagnetic work revealed that only slight translation movement has occurred between the neighboring Tarim Basin and Turpan Basin since the Cretaceous, suggesting that the Tarim Basin and Turpan-Hami Basin have been largely influenced by the same arid belt produced by the subtropical high from 145 Ma to 66 Ma (Cogné et al., 1995), although potentially impacted by much different orography. The divergent axis of the subtropical high-pressure belt is the boundary position of the westerlies and northeast trade winds (Hasegawa et al., 2012; Wang et al., 2023). The westerly wind direction suggests that the Hami Basin is located north of the divergence axis of the subtropical high (e.g., Hasegawa et al., 2012). The location of the Hami Basin in the arid climate belt under the predominant influence of the subtropical high system favors the development of the Liushuquan erg. The rain shadow effect created by the orogenic belt can impede the movement of ocean water vapor to the inland basins (Li et al., 2018). However, the effect of the paleo-Tianshan mountains on the Early Cretaceous aridity and eolian expansion is limited (Wang et al., 2023). The Late Jurassic-Early Cretaceous deposits on both sides of Tianshan suggest that a long-term semi-arid to arid climate condition existed at that time (Jolivet et al., 2017).

The uplift of the eastern Tianshan increased exhumation and provided a source for the Early Cretaceous sediments in the Hami Basin (Shen et al., 2020). The characteristics of the basin area and source rocks of the Turpan-Hami Basin are closely associated with the uplift of the eastern Tianshan during the Cretaceous. Sandy deserts typically form in basins with extensive accumulation space, whereas a salient limitation for desert development in intermountain basins is their restricted accumulation space (Cao et al., 2020; Zheng et al., 2024). The late Mesozoic

mountain-building processes formed the largest intermountain basin within the Tianshan, encompassing an area of 5350 km² (Jiang et al., 2015). This enclosed basin provided a much larger accumulation space for eolian sands compared to the intermountain basins in South China, where Late Cretaceous ergs developed (e.g., Wu et al., 2018; Huang et al., 2019; Cao et al., 2020, 2023; Yu et al., 2020, 2021a). These Late Cretaceous basins in South China varied in size from dozens to hundreds of square kilometers, with some exceeding 1000 km² (Zheng et al., 2024). Drilling cores reveal that the Liushuquan erg predominantly occupies the central and northern parts of our study area located at the southern edge of the Turpan-Hami Basin (Figs. 2 and 10). A Paleozoic bulge (Wang et al., 2020) impeded the southern expansion of these eolian sands. The cores indicate a northward increase in eolian deposit thickness (Fig. 10), suggesting the possibility of more substantial eolian deposits in the center of the Hami Basin. Seismic profiles reveal a progressive increase in the thickness of post-Jurassic sediments from the south to the north across the entire Hami Basin (Jiang et al., 2015).

Paleo-Winds and Atmospheric Circulation Patterns in Asia during the Early Cretaceous

Paleo-atmospheric forcing and tectonics are the two dominant factors in the formation of ergs during the Early Cretaceous in Central and East Asia. The Late Jurassic to Early Cretaceous Lhasa-Qiangtang and Mongol-Okhotsk collisions (Kapp et al., 2005; Yang et al., 2015) resulted in extensive topographic uplift in SE Tibet to the west (Hu et al., 2020; Wu et al., 2023) and the Pamir Plateau and Tianshan to the north (Tang et al., 2015; Gillespie et al., 2017; Chapman et al., 2018). During the Late Cretaceous, a north-south oriented coastal mountain was uplifted due to the northwestward subduction of the paleo-Pacific plate beneath the paleo-Asian continent (Li et al., 2019; Clinkscales et al., 2021; Zhang et al., 2021). These elevated mountains hindered moisture from the Meso- and Neo-Tethys oceans, the Paleo-Pacific Ocean, and the north polar regions from entering the interior of East Asia (Zhang et al., 2021; Wang et al., 2023; Wu et al., 2023). Aside from tectonics as a driving mechanism, shifts in the subtropical high-pressure belt in response to changing climate conditions led to migrations of deserts and prevailing surface-wind patterns during the Cretaceous (Hasegawa et al., 2012; Qiao et al., 2022; Wu et al., 2023). Before the uplift of the Tibetan Plateau, which affects the mid-latitude westerly wind belt, the Cretaceous climate of East Asia was more widely associated with perturbations related to shifts in Hadley circulation (Liu et al., 1998). Particularly, the prevailing lower-level winds during the Cretaceous were probably more directly related to the latitude of synoptic wind belts than present-day (Qiao et al., 2022). The Cretaceous erg deposits in Central and East Asia are primarily associated with sustained aridity beneath the descending limb of the subtropical Hadley Cell (Jiang and Li, 1996; Jiang et al., 2001; Hasegawa et al., 2010, 2012; Wu et al., 2017; Yu et al., 2020). As such, the spatiotemporal changes of desert distributions and the prevailing surface wind patterns recorded in the stratigraphic record can be used to infer the migration of synoptic winds (Hasegawa et al., 2012; Li et al., 2018; Wu et al., 2018; Yu et al., 2020, 2021a; Qiao et al., 2022). Taking a regional perspective, we use published magnetostratigraphic, biostratigraphic, and isotope chronologic data to constrain the depositional ages of Early Cretaceous eolianites in East Asia (Fig. 11). The paleo-latitudes of the basins containing the eolianites of this age have been well documented (see Hasegawa et al., 2012, and Xu et al., 2013, and references therein). In the following paragraph, we consider paleoatmospheric circulation and the superposition of topographic effects in the forcing of widespread eolianite accumulation and prevailing patterns during the Early Cretaceous (Figs. 11 and 12).

The data presented here, along with previously published observations, allow us to propose a three-stage model for synoptic winds over East Asia during the Early Cretaceous. The zonal boundary between the westerlies, trade winds, and the subtropical high during the Cretaceous can be reconstructed here based on the paleowind data (Hasegawa et al., 2012). During the earliest Cretaceous (late Berriasian-Valanginian), the paleo-wind data show that the Hami Basin, Shangyi Basin, and Chaoyang-Beipiao Basin were under the influence of lower-level westerly winds (a, e, and f in Fig. 12A; Xu et al., 2013). The paleo-currents in the upper part of the Yijinhuoluo Formation and the lower part of the Luohe Formation in the Ordos Basin indicate a switch or alternation between predominately lower-level westerly and easterly wind directions (b, c, and d in Fig. 12A; Jiang et al., 2001; Qiao et al., 2022). We infer the mean position of the subtropical high to have been located around the latitude of the Ordos Basin and infer that the subtropical high has drifted south and north to explain the spatial variations in paleo-current data (Fig. 12A; Jiang et al., 2001). The paleocurrent data suggest that lower-level westerlies persisted during the deposition of the upper part of the Luohe Formation in the Ordos Basin in the Valanginian (Jiang et al., 2001; Qiao et al., 2022). This is associated with a stabilization of

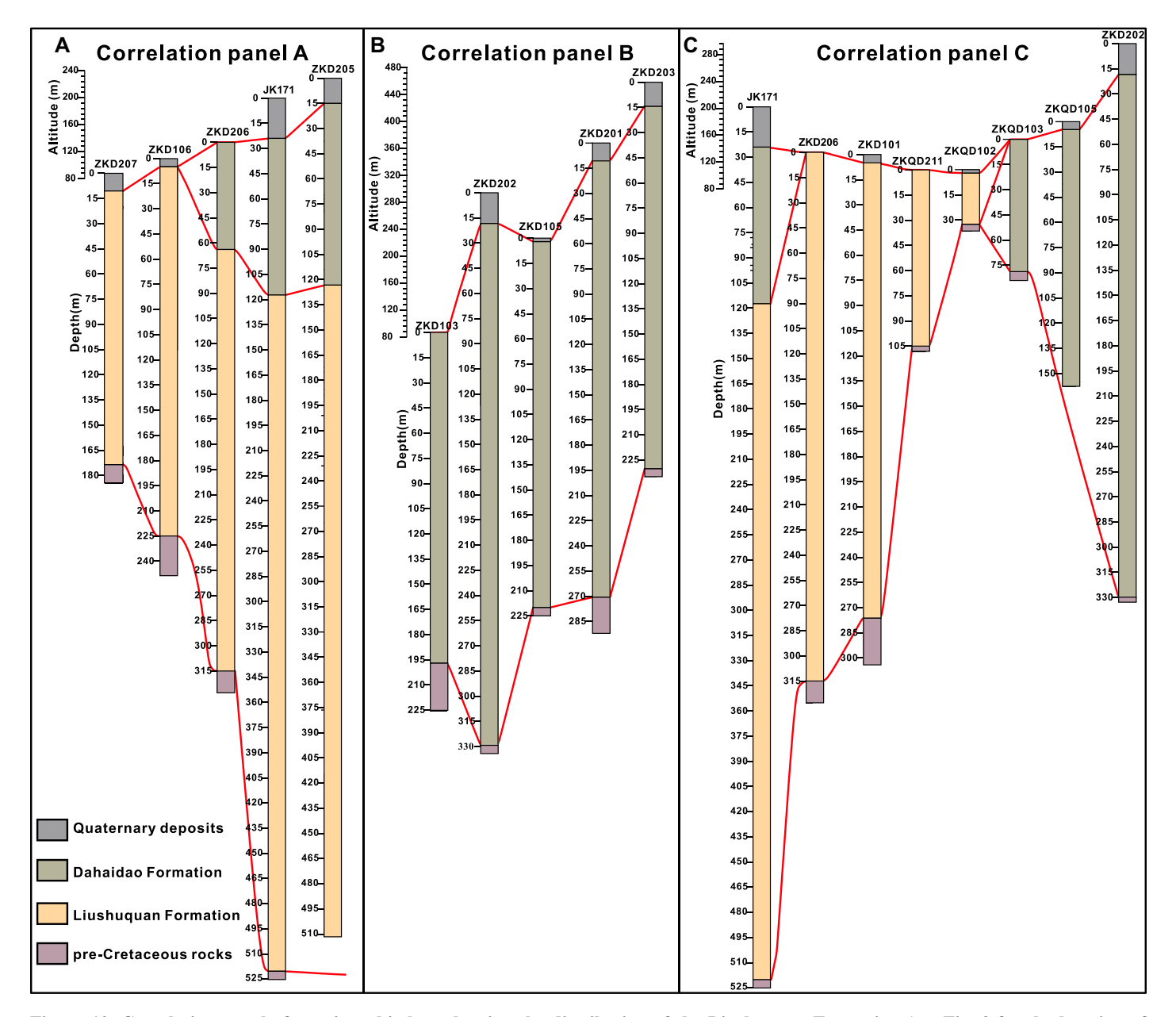


Figure 10. Correlation panel of stratigraphic logs showing the distribution of the Liushuquan Formation (see Fig. 2 for the location of boreholes).

the synoptic wind belts during this interval, with the subtropical high more consistently located around the latitude of the southern Ordos Basin (Jiang et al., 2001; Qiao et al., 2022). In summary, during the earliest Cretaceous, the subtropical high belt drifted southward and northward over shorter time scales within the spatial domain of the paleo-Ordos Basin, then consistently located around the paleo-latitude of the southern Ordos Basin (Fig. 11A). Several lines of evidence suggest that the Lhasa-Qiangtang collision occurred during 150–130 Ma (Li et al., 2019), leading to the deformation and shortening of the Qiangtang and Lhasa terranes as well as the crustal thick-

ening and probable uplift of southern Tibet during the Early Cretaceous (Murphy et al., 1997). However, the paleo-elevation of the southern Tibetan Plateau was still probably <2000 m until 125 Ma (Hu et al., 2020). Influenced by the Lhasa-Qiangtang and Mongol-Okhotsk collisions, Tianshan also experienced crustal thickening and uplift prior to the Cenozoic (Tang et al., 2015; Chapman et al., 2018). However, the Tianshan remained very limited up to the late Cenozoic (Jolivet et al., 2017), contradicting the rain-shadow effect driven by surface uplift on mid-latitude aridity (Wang et al., 2023). The presence of permafrost preserved within the Luohe

Formation indicates a paleo-altitude of 3–4 km in the central Ordos Basin (Rodríguez-López et al., 2022). Its location beneath the subtropical high-pressure zone, where drought prevailed, suggests that the aridity was tightly linked to atmospheric circulation, as well as to the superposition of topographic effects. The consistent westerly winds in the Ordos Basin indicate that the elevated plateau did not transform the prevailing surface wind pattern (Jiang et al., 2001; Qiao et al., 2022; Rodríguez-López et al., 2022). Toward the middle stage of the Early Cretaceous (late Hauterivian–Barremian), the Luohandong Formation records westerly winds in the Ordos

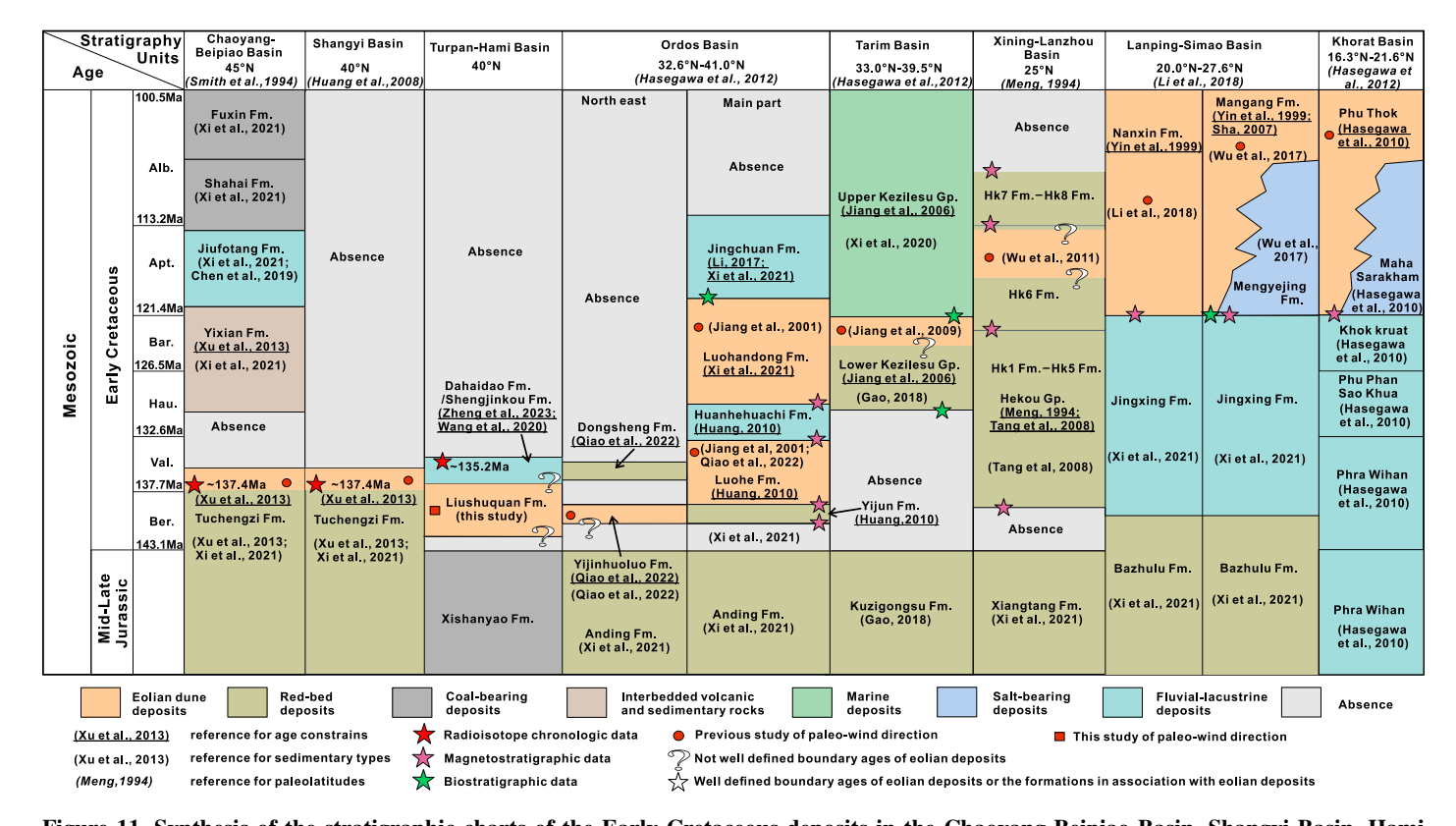


Figure 11. Synthesis of the stratigraphic charts of the Early Cretaceous deposits in the Chaoyang-Beipiao Basin, Shangyi Basin, Hami Basin, Ordos Basin, Tarim Basin, Xining-Lanzhou Basin, Lanping-Simao Basin, and Khorat Basin of China and Thailand. The Cretaceous time scale is from the Geologic Time Scale 2020 (Gale et al., 2020). The deposition ages based on biostratigraphic, magnetostratigraphic, and radioisotope chronologic data are cited from Meng (1994), Yin et al. (1999), Jiang et al. (2006), Sha (2007), Tang et al. (2008), Hasegawa et al. (2010), Huang (2010), Xu et al. (2013), Li (2017), Wang et al. (2020), and Xi et al. (2021). Sedimentary types are cited from Jiang et al. (2001, 2009), Tang et al. (2008), Hasegawa et al. (2010), Xu et al. (2013), Wu et al. (2017), Gao (2018), Li et al. (2018), Chen et al. (2019), Wang et al. (2020), Xi et al. (2020, 2021), and Qiao et al. (2022). Paleo-latitudes are based on paleomagnetic studies by Meng (1994), Smith et al. (1994), Huang et al. (2008), Hasegawa et al. (2012, and references therein), Li et al. (2018, and references therein), and Zheng et al. (2023). Fm.—Formation; Alb.—Albian; Apt.—Aptian; Bar.—Barremian; Hau.—Hauterivian; Val.—Valanginian; Ber.—Berriasian.

Basin, while the Kezilesu Group in the northwestern Tarim Basin records primarily easterly winds (Figs. 11 and 12C; Jiang et al., 2001, 2009). The small latitudinal difference coupled with clear differences in winds may be evidence that this latitude was close to the boundary between the lower-level westerlies and easterlies (Fig. 12C). Meso-Tethys seawater totally withdrew between the Oiangtang and Lhasa terranes after 125 Ma (Kapp et al., 2005; Wang et al., 2023), showing that the retreat of the Meso-Tethys Ocean and uplift of the Qiangtang and Lhasa terranes decreased moisture input into the Tarim Basin and induced erg deposition (Fig. 12D). Eolianites in the East Asian stratigraphic record shift south in the Aptian-Albian while higher latitude basins became wetter (Fig. 11). Because the rainshadow effect driven by progressive collision and topographic uplift in inland Asia was irreversible. this scenario is inconsistent with the transition from arid to relatively humid conditions (Wang et al., 2023). We suggest that the location of the subtropical high-pressure zone primarily controlled the formation of the mid-latitude desert belt and its wind pattern, although this impact may have been superimposed on topographic effects during this interval. During the Aptian— Albian, paleo-wind directions in the upper Hekou Group indicate that the Xining-Lanzhou Basin was primarily subjected to lower-level westerly winds (Fig. 12D; Wu et al., 2011), which corresponds with the desert in the Sichuan Basin also being predominately westerly with some northeasterly trade winds (Fig. 12E; Jiang et al., 1999). Eolianites recorded to the south of the Sichuan Basin in the Lanping-Simao Basin and Krout Basin indicate geomorphically effective lower-level easterly winds (Hasegawa et al., 2010; Wu et al., 2017; Li et al., 2018). The variation in depositional environments toward more lacustrine and coal-bearing deposits in basins to the north indicates a prevailing humid climate during the Aptian-Albian (Wu et al., 2018; Wu and Rodríguez-López, 2021). The changes in the distribution of deserts, prevailing surface-wind patterns, and depositional environment suggest a general equatorward contraction of the synoptic wind belts, putting the Sichuan Basin closer to the core of the subtropical high during the Aptian-Albian (Fig. 11E). During the Early Cretaceous (ca. 125-100 Ma), the Southern Qiangtang and Northern Lhasa terranes were uplifted from \sim 2000 m to 3000 m, and the paleo-elevation of the Southern Lhasa terrane was relatively stable at 2500 m (Hu et al., 2020). Paleotopography construction based on thermal modeling and provenance analysis shows that the SE Tibetan Plateau initially formed a growing N-S-trending barrier (e.g., Qiangtang-Lhasa terranes and Indochina mountains) since the Aptian-Albian (Wu et al., 2023), which played an important role in the Aptian-Albian aridification in the low-latitude basins (Fig. 12F). However, the low-altitude Lancangjiang tectonic zone between Qiangtang-Lhasa terranes and Indochina mountains during this period left a huge gap for moisture transmis-

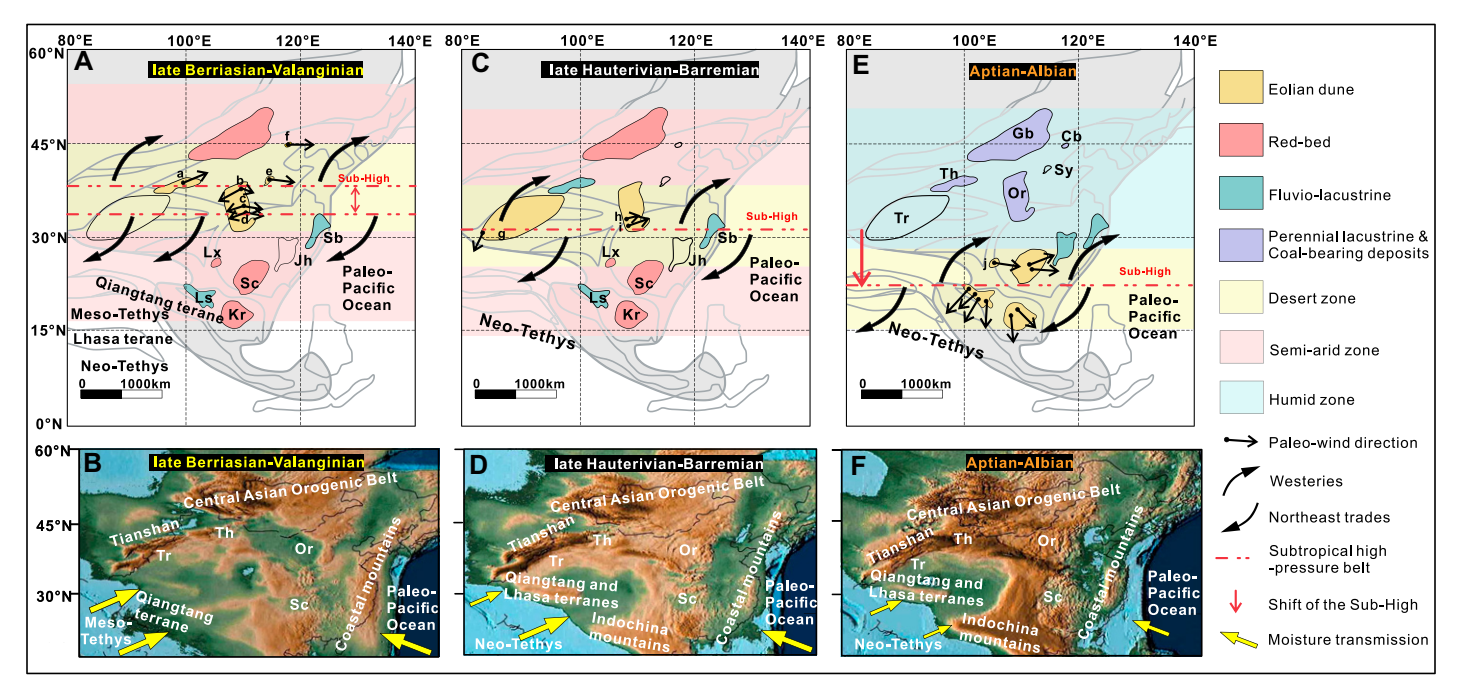


Figure 12. Paleogeographic map of the Asian continent during the Early Cretaceous, showing the locations of sedimentary basins, shifts in subtropical high-pressure belts, and major mountain building processes. Panels A, C, and E are modified from Hasegawa et al. (2012) and Yu et al. (2021b). Panels B, D, and F are modified from Scotese (2016) and Wu et al. (2023). Cb—Chaoyang-Beipiao Basin; Jh—Jianghan Basin; Kr—Khorat Basin; Ls—Lanping-Simao Basin; Lx—Lanzhou-Xining Basin; Or—Ordos Basin; Sb—Subei Basin; Sc—Sichuan Basin; Sy—Shangyi Basin; Th—Turpan-Hami Basin; Tr—Tarim Basin. a—westerly winds from the Liushauuqan Formation (this study); b—transition from easterly to westerly winds from the Yijinhuoluo Formation (Qiao et al., 2022); c—alternation of easterly and westerly winds from the Luohe Formation (Jiang et al., 2001); e—westerly winds from the Tuchengzi Formation (Xu et al., 2013); f—westerly winds from the Tuchengzi Formation (Xu et al., 2013); g—easterly winds from the Kezilesu Group (Jiang et al., 2009); h and i—westerly winds from the Luohandong Formation; j—westerly winds from the Hekou Group. The paleo-wind directions of the Sichuan, Lanping-Simao, and Khorat basins are from Li et al. (2018).

sion (Fig. 12F; Wu et al., 2023). The subtropical high-pressure systems and topographic conditions jointly resulted in an arid climate and ergs deposition in the low-latitude regions during the Aptian–Albian (Figs. 12E and 12F).

The role of the topographic effect in regional and global aridification was limited during the Early Cretaceous (Wang et al., 2023). The spatially differential mountain-building processes over East Asia cannot fully explain the latitudinal distribution and consistent migration of deserts and prevailing surface-wind patterns (Qiao et al., 2022; Wang et al., 2023). The topographic upliftdriving aridification should have been to some extent irreversible (Wang et al., 2023), so the arid to humid climate changes in the Hami and Ordos basins during the Early Cretaceous (Qiao et al., 2022) cannot be only attributed to the collisioninduced surface uplift. Until the Late Cretaceous, the topographic effect in East Asia had a dominant influence on the paleoclimate of some local low-latitude basins (i.e., Lanping Basin; Wu et al., 2023), even when the westerlies or subtropicalhigh pressure system moved away (Hasegawa et al., 2012). Therefore, although the interaction

between paleo-atmosphere dynamics and tectonic forcing eventually determines the formation of desert systems (Wu et al., 2018), we suggest that atmosphere dynamics were the dominant factor in the latitude distribution and migration of east Asian erg belts until the Late Cretaceous, when topographic effects trigger the formation of eolian deserts locally (Wu et al., 2023).

We recognize that this model is perhaps oversimplistic, as it diminishes the potential impacts of complexities like topographic effects on lower-level winds, which we note above. However, at this point, it may be difficult to completely integrate the interaction between subtropical high-pressure systems and topographic conditions due to its local variations over East Asia. To that end, we chose to focus on direct analysis of the stratigraphic record and recognize that this model may require refining as those uncertainties diminish.

CONCLUSION

The existence of an Early Cretaceous (late Berriasian–early Valanginian) erg system in the East Asia interior (Hami Basin) is demonstrated based on the sedimentological study of the Early Cretaceous Liushuquan Formation, which was originally considered to be fluviallacustrine deposits. The development of Liushuquan erg is tightly associated with the hot and arid climate controlled by the subtropical high-pressure systems and some orographic blocking. The mean azimuth of the foresets of the large-scale cross-bedded sandstones after magnetic deviation correction (82.6°) indicates that the prevailing lower-level winds in the Hami Basin were westerlies. We used data from the Early Cretaceous Liushuquan Formation along with other data from East Asia to propose a new three-stage model aimed at resolving migrations in the subtropical high and synoptic winds over that interval. In summary, the model proposed here suggests (1) the subtropical high shifted southward and northward within the spatial domain of the paleo-Ordos Basin during the late Berriasian to Valanginian, (2) stabilization of the Hadley Cell with the subtropical high centered at the southern margin of the paleo-Ordos Basin during the late Hauterivian to Barremian, and (3) a notable southward shift in the subtropical high to the middle of the paleo-Sichuan and paleo-Lanping-Simao basins with a marked increase in humidity at the higher latitudes (\sim 32°–50°N) during the Aptian–Albian.

ACKNOWLEDGMENTS

This research is financially supported by the National Natural Science Foundation of China (grant nos. 42172251, 41972208, 42274105, and U22B6002), the China Geological Survey (grant nos. DD20179607 and DD20160060), the Third Xinjing Scientific Expedition Program (grant no. 2023xjkk0105-3), the State Key Laboratory of Earth System Science, Yunnan University, open project fund (grant no. ESS2023001), and the U.S. National Science Foundation (grant no. 1545859). J.T. Abell is currently supported by a National Science Foundation—Ocean Sciences Postdoctoral Fellowship (#2126500). The authors thank Brad Singer, Alessandro Zanazzi, and four anonymous reviewers for comments that greatly improved the manuscript.

REFERENCES CITED

- Allen, M.B., Windley, B.F., Zhang, C., and Guo, J., 1993, Evolution of the Turfan Basin, Chinese Central Asia: Tectonics, v. 12, p. 889–896, https://doi.org/10.1029/93TC00598.
- Allen, M.B., Windley, B.F., and Zhang, C., 1994, Cenozoic tectonics in the Urumgi-Korla region of the Chinese Tien Shan: Geologische Rundschau, v. 83, p. 406–416, https://doi.org/10.1007/BF00210554.
- Al-Masrahy, M.A., and Mountney, N.P., 2015, A classification scheme for fluvial-aeolian system interaction in desert-margin settings: Aeolian Research, v. 17, p. 67–88, https://doi.org/10.1016/j.aeolia.2015.01.010.
- An, Z., Kutzbach, J.E., Prell, W.L., and Porter, S.C., 2001, Evolution of Asian monsoons and phased uplift of the Himalaya-Tibetan plateau since Late Miocene times: Nature, v. 411, p. 62–66, https://doi.org/10.1038 /35075035.
- Brookfield, M., and Silvestro, S., 2010, Eolian systems, *in* Dalrymple, R.W., and James, N.P., eds., Facies Models: St. John's, Newfoundland, Canada, Geological Association of Canada, p. 139–166.
- Cao, S., Zhang, L., Wang, C., Ma, J., Tan, J., and Zhang, Z., 2020, Sedimentological characteristics and aeolian architecture of a plausible intermountain erg system in Southeast China during the Late Cretaceous: Geological Society of America Bulletin, v. 132, p. 2475–2488, https://doi.org/10.1130/B35494.1.
- Cao, S., Ma, J., and Wang, C., 2023, The sedimentological characteristics of the intermontane desert system in the Jurong Basin, South China and its relationship with the Late Cretaceous hot climate: Palaeogeography, Palaeoclimatology, Palaeoecology, v. 623, https://doi.org/10 .1016/j.palaeo.2023.111618.
- Chapman, J.B., Robinson, A.C., Carrapa, B., Villarreal, D., Worthington, J., DeCelles, P.G., Kapp, P., Gadoev, M., Oimahmadov, I., and Gehrels, G., 2018, Cretaceous shortening and exhumation history of the South Pamir terrane: Lithosphere, v. 10, p. 494–511, https://doi.org/10.1130/L691.1.
- Chen, G., Zhang, X., Yang, G., Han, G., Bian, J., Yang, Y., and Zhuo, S., 2019, Sedimentary and organic matter characteristics of Lower Cretaceous Jiufotang Formation in western Liaoning Province: Dizhi Tongbao, v. 38, p. 426–436.
- Chen, Y., Wang, G., Kapp, P., Shen, T., Zhang, P., Zhu, C., and Cao, K., 2020, Episodic exhumation and related tectonic controlling during Mesozoic in the Eastern Tian Shan, Xinjiang, northwestern China: Tectonophysics, v. 796, https://doi.org/10.1016/j.tecto.2020.228647.
- Chen, Z., Wang, Z., Han, F., Zhang, W., Zhang, Q., Zhou, Z., Wang, X., Xiao, W., Han, S., Yu, X., Sun, Y., Nurgazy, T., Latyshev, N., and Zailabidin, H., 2018, Late Cre-

- taceous—Cenozoic uplift, deformation, and erosion of the SW Tianshan Mountains in Kyrgyzstan and Western China: International Geology Review, v. 60, p. 1019– 1037, https://doi.org/10.1080/00206814.2017.1365018.
- Cheng, J., Jiang, F., Xue, C., Xin, G., Li, K., and Yang, Y., 2015, Characteristics of the disastrous wind-sand environment along railways in the Gobi area of Xinjiang, China: Atmospheric Environment, v. 102, p. 344–354, https://doi.org/10.1016/j.atmosenv.2014.12.018.
- Clinkscales, C., Kapp, P., Thomson, S., Wang, H., Laskows-ki, A., Orme, D.A., and Pullen, A., 2021, Regional exhumation and tectonic history of the Shanxi Rift and Taihangshan, North China: Tectonics, v. 40, https://doi.org/10.1029/2020TC006416.
- Cogné, J.P., Chen, Y., Courtillot, V., Rocher, F., Wang, G., Bai, M., and You, H., 1995, A Paleomagnetic study of Mesozoic sediments from the Junggar and Turfan basins, northwestern China: Earth and Planetary Science Letters, v. 133, no. 3–4, p. 353–366, https://doi.org/10 .1016/0012-821X(95)00083-O.
- DeCelles, P.G., Kapp, P., Ding, L., and Gehrels, G.E., 2007a, Late Cretaceous to middle Tertiary basin evolution in the central Tibetan Plateau: Changing environments in response to tectonic partitioning, aridification, and regional elevation gain: Geological Society of America Bulletin, v. 119, p. 654–680, https://doi.org/10.1130/B26074.1.
- DeCelles, P.G., Quade, J., Kapp, P., Fan, M., Dettman, D.L., and Ding, L., 2007b, High and dry in central Tibet during the Late Oligocene: Earth and Planetary Science Letters, v. 253, no. 3–4, p. 389–401, https://doi.org/10.1016/j.epsl.2006.11.001.
- De Pelsmaeker, E., Jolivet, M., Laborde, A., Poujol, M., Robin, C., Zhimulev, F.I., Nachtergaele, S., Glorie, S., De Clercq, S., Batalev, V.Y., and De Grave, J., 2018, Source-to-sink dynamics in the Kyrgyz Tien Shan from the Jurassic to the Paleogene: Insights from sedimentological and detrital zircon U-Pb analyses: Gondwana Research, v. 54, p. 180–204, https://doi.org/10.1016/j .gr.2017.09.004.
- do Amarante, F.B., Scherer, C.M.S., Aguilar, C.A.G., Dos Reis, A.D., Mesa, V., and Soto, M., 2019, Fluvial-eolian deposits of the Tacuarembo formation (Norte Basin– Uruguay): Depositional models and stratigraphic succession: Journal of South American Earth Sciences, v. 90, p. 355–376, https://doi.org/10.1016/j.jsames 2018.12.024
- Eberth, D.A., Brinkman, D.B., Chen, P., Yuan, F., Wu, S., Li, G., and Cheng, X., 2001, Sequence stratigraphy, paleoclimate patterns, and vertebrate fossil preservation in Jurassic–Cretaceous strata of the Junggar Basin, Xinjiang Autonomous Region, People's Republic of China: Canadian Journal of Earth Sciences, v. 38, no. 12, p. 1627–1644, https://doi.org/10.1139/cjes-38 -12-1627.
- Fang, Y., Wu, C., Wang, Y., Hou, K., and Guo, Z., 2019, Topographic evolution of the Tianshan Mountains and their relation to the Junggar and Turpan Basins, Central Asia, from the Permian to the Neogene: Gondwana Research, v. 75, p. 47–67, https://doi.org/10.1016/j.gr 2019.03.020.
- Folk, R.L., and Ward, W.C., 1957, Brazos river bar: A study in the significance of grain size parameters: Journal of Sedimentary Petrology, v. 27, p. 3–26, https://doi.org /10.1306/74D70646-2B21-11D7-8648000102C1865D.
- Friedman, G.M., 1961, Distinction between dune, beach, and river sands from their textural characteristics:
 Journal of Sedimentary Research, v. 31, p. 514–529, https://doi.org/10.1306/74D70BCD-2B21-11D7-8648000102C1865D.
- Friedman, G.M., 1967, Dynamic processes and statistical parameters compared for size frequency distribution of beach and river sands: Journal of Sedimentary Research, v. 37, p. 327–354, https://doi.org/10.1306 //4D716CC-2B21-11D7-8648000102C1865D.
- Gale, A.S., Mutterlose, J., Batenburg, S.J., Gradstein, F.M., Agterberg, F.P., Ogg, J.G., and Petrizzo, M.R., 2020, The Cretaceous period, in Gradstein, F.M., Ogg, J.G., Schmitz, M.D., and Ogg, G.M., eds, Geologic Time Scale 2020: Amsterdam, Elsevier, p. 1023–1086, https://doi.org/10.1016/B978-0-12-824360-2.00027-9.
- Gao, H., Liu, H., He, J., Tian, M., and Che, Y., 2014, Mesozoic-Cenozoic uplift-exhumation history of East

- Tianshan: Evidence from apatite fission track: Earth Science Frontiers, v. 21, p. 249–260.
- Gao, R., 2018, Mineralization of Mesozoic–Cenozoic sandstone-hosted Zn-Pb deposits in the southwestern Tianshan, Xinjiang, NW China: Exemplified by the Uragen Zn-Pb deposit [Ph.D. thesis]: Beijing, China, China University of Geosciences (Beijing), 147 p.
- Garzione, C.N., 2008, Surface uplift of Tibet and Cenozoic global cooling: Geology, v. 36, p. 1003–1004, https://doi.org/10.1130/focus122008.1.
- Gillespie, J., Glorie, S., Jepson, G., Zhang, Z.Y., Xiao, W.J., Danišík, M., and Collins, A.S., 2017, Differential exhumation and crustal tilting in the Easternmost Tianshan (Xinjiang, China), revealed by low-temperature thermochronology: Tectonics, v. 36, p. 2142–2158, https://doi.org/10.1002/2017TC004574.
- Hadlari, T., Rainbird, R.H., and Donaldson, J.A., 2006, Alluvial, eolian and lacustrine sedimentology of a Paleoproterozoic half-graben, Baker Lake Basin, Nunavut, Canada: Sedimentary Geology, v. 190, p. 47–70, https://doi.org/10.1016/j.sedgeo.2006.05.005.
- Hasegawa, H., Tada, R., Ichinnorov, N., and Minjin, C., 2009, Lithostratigraphy and depositional environments of the upper cretaceous Djadokhta formation, Ulan Nuur Basin, southern Mongolia, and its paleoclimatic implication: Journal of Asian Earth Sciences, v. 35, p. 13–26, https://doi.org/10.1016/j.jseaes.2008.11.010.
- Hasegawa, H., Imsamut, S., Charusiri, P., Tada, R., Horiuchi, Y., and Hisada, K.I., 2010, 'Thailand was a desert' during the mid-Cretaceous: Equatorward shift of the subtropical high-pressure belt indicated by eolian deposits (Phu Thok Formation) in the Khorat Basin, northeastern Thailand: The Island Arc, v. 19, p. 605–621, https://doi.org/10.1111/j.1440-1738.2010.00728.x.
- Hasegawa, H., Tada, R., Jiang, X., Suganuma, Y., Imsamut, S., Charusiri, P., Ichinnorov, N., and Khand, Y., 2012, Drastic shrinking of the Hadley circulation during the mid-Cretaceous Supergreenhouse: Climate of the Past, v. 8, p. 1323–1337, https://doi.org/10.5194/cp-8 -1323-2012.
- He, Z., Wang, B., Glorie, S., Su, W., Ni, X., Jepson, G., Liu, J., Zhong, L., Gillespie, J., and De Gravel, J., 2022, Mesozoic building of the Eastern Tianshan and East Junggar (NW China) revealed by low-temperature thermochronology: Gondwana Research, v. 103, p. 37–53, https://doi.org/10.1016/j.gr.2021.11.013.
- Hendrix, M.S., Graham, S.A., Carroll, A., Sobel, E., McKnight, C., Schulein, B., and Wang, Z., 1992, Sedimentary record and climatic implications of recurrent deformation in the Tian Shan: Evidence from Mesozoic strata of the North Tarim, south Dzungar, and Turpan basin, Northwest China: Geological Society of America Bulletin, v. 104, p. 53–79, https://doi.org/10.1130/0016-7606(1992)104<0053:SRACIO>2.3.CO;2.
- Hu, F., Wu, F., Chapman, J.B., Ducea, M.N., Ji, W., and Liu, S., 2020, Quantitatively tracking the elevation of the Tibetan Plateau since the Cretaceous: Insights from whole rock Sr/Y and La/Yb ratios: Geophysical Research Letters, v. 47, https://doi.org/10.1029/2020GL089202.
- Huang, B., Zhou, Y., and Zhu, R., 2008, Discussions on Phanerozoic evolution and formation of continental China, based on paleomagnetic studies: Earth Science Frontiers, v. 15, p. 348–359.
- Huang, L., Huang, J., Luo, L., Wang, X., Liu, Y., Liang, E., and Ma, H., 2019, The discovery of Cretaceous eolian deposits at the eastern margin of the Hengyang Basin, Hunan, and its paleoenvironmental significance: Acta Sedimentologica Acta, v. 37, p. 735–747.
- Huang, Y., 2010, The origin and evolution of the desert in southern Ordos in early Cretaceous: Constraint from magnetostratigraphy of Zhidan Group and magnetic susceptibility and its sediment [M.S. thesis]: Lanzhou, China, Lanzhou University, 78 p.
- Hunter, R.E., 1977, Basic types of stratification in small eolian dunes: Sedimentology, v. 24, p. 361–387, https://doi.org/10.1111/j.1365-3091.1977.tb00128.x.
- Jiang, D., Wang, Y., He, Z., Dong, K., Ni, Q., and Tian, N., 2006, Early Cretaceous palynofloras from the Kizilsu Group in the Tarim Basin, Xinjiang: Acta Micropalaeontologica Sinica, v. 23, no. 4, p. 371-391.
- Jiang, S., Li, S., Somerville, I.D., Lei, J., and Yang, H., 2015, Carboniferous–Permian tectonic evolution and

- sedimentation of the Turpan-Hami Basin, NW China: Implications for the closure of the Paleo-Asian Ocean: Journal of Asian Earth Sciences, v. 113, p. 644–655, https://doi.org/10.1016/j.jseaes.2015.05.012.
- Jiang, X., and Li, Y., 1996, Spato-temporal distribution of the Cretaceous desert in central and eastern China and its climatic significance: Sedimentary Facies and Palaeogeography, v. 16, p. 42–51.
- Jiang, X., Pan, Z., and Fu, Q., 1999, The variations of palaeowind direction of the Cretaceous desert in the Sichuan Basin and their significance: Sedimentary Facies and Palaeogeography, v. 19, no. 1, p. 1–11.
- Jiang, X., Pan, Z., and Fu, Q., 2001, Regularity of palaeowind directions of the early Cretaceous desert in Ordos Basin and climatic significance: Science in China Series D: Earth Sciences, v. 44, p. 24–33, https://doi.org/10.1007 //BF02906882.
- Jiang, X., Cai, X., Pan, Z., Xiong, G., and Wu, H., 2009, Paleowind direction measurements and paleowind belt reconstruction of the Early Cretaceous eolian dunes in southwestern Tarim Basin, Xinjiang: Chenji Yu Tetisi Dizhi, v. 29, p. 1–4.
- Jiao, H., Wu, C., Rodríguez-Lópezc, J.P., Sun, X., and Yi, H., 2020, Late Cretaceous plateau deserts in the South China Block, and Quaternary analogues; sedimentology, dune reconstruction and wind-water interactions: Marine and Petroleum Geology, v. 120, https://doi.org /10.1016/j.marpetgeo.2020.104504.
- Jo, H.R., Rhee, C.W., and Chough, S.K., 1997, Distinctive characteristics of a stream flow dominated alluvial fan deposit: Sanghori area, Kyongsang Basin (Early Cretaceous), southeastern Korea: Sedimentary Geology, v. 110, p. 61–79, https://doi.org/10.1016/S0037 -0738(96)00083-8.
- Jolivet, M., Bourquin, S., Heilbronn, G., Robin, C., Barrier, L., Dabard, M.P., Jia, Y., De Pelsmaeker, E., and Fu, B., 2017, The Upper Jurassic–Lower Cretaceous alluvialfan deposits of the Kalaza Formation (Central Asia): Tectonic pulse or increased aridity?, in Brunet, M.-F., McCann, T., and Sobel, E.R., eds., Geological Evolution of Central Asian Basins and the Western Tien Shan Range: Geological Society, London, Special Publication 427, p. 491–521, https://doi.org/10.1144/SP427.6.
- Jones, F.H., Scherer, C.M.S., and Kuchle, J., 2016, Facies architecture and stratigraphic evolution of aeolian dune and interdune deposits, Permian Caldeirão Member (Santa Brígida Formation), Brazil: Sedimentary Geology, v. 337, p. 133–150, https://doi.org/10.1016/j.sedgeo.2016.03.018.
- Kapp, P., Yin, A., Harrison, T.M., and Ding, L., 2005, Cretaceous-Tertiary shortening, basin development, and volcanism in central Tibet: Geological Society of America Bulletin, v. 117, p. 865–878, https://doi.org/10.1130 /B25595.1.
- Kocurek, G., 1981, Significance of interdune deposits and bounding surfaces in aeolian dune sands: Sedimentology, v. 28, p. 753–780, https://doi.org/10.1111/j.1365-3091.1981.tb01941.x.
- Kocurek, G., 1991, Interpretation of ancient eolian sand dunes: Annual Review of Earth and Planetary Sciences, v. 19, p. 43–75, https://doi.org/10.1146/annurev.ea.19 .050191.000355.
- Kocurek, G., 1996, Desert aeolian systems, in Reading, H.G., ed., Sedimentary Environments: Processes, Facies and Stratigraphy: Oxford, UK, Blackwell Science, p. 125–153.
- Kutzbach, J.E., Prell, W.L., and Ruddiman, W.F., 1993, Sensitivity of Eurasian climate to surface uplift of the Tibetan Plateau: The Journal of Geology, v. 101, no. 2, p. 177–190, https://doi.org/10.1086/648215.
- Li, G., 2017, SEM morphological study of the type species of Ordosestheria Wang, 1984 (Spinicaudata) from Ordos Basin of mid-west China: Cretaceous Research, v. 75, p. 1–6, https://doi.org/10.1016/j.cretres.2017.03.006.
- Li, G., Wu, C., Rodríguez–López, J.P., Yi, H., Xia, G., and Wagreich, M., 2018, Mid-Cretaceous aeolian desert systems in the Yunlong area of the Lanping Basin, China: Implications for palaeoatmosphere dynamics and paleoclimatic change in East Asia: Sedimentary Geology, v. 364, p. 121–140, https://doi.org/10.1016/j .sedgeo.2017.12.014.
- Li, P., Sun, M., Rosenbaum, G., Cai, K., Yaun, C., Jourdan, F., Xia, X., Jiang, Y., and Zhang, Y., 2020, Tectonic

- evolution of the Chinese Tianshan Orogen from subduction to arc-continent collision: Insight from polyphase deformation along the Gangou section, Central Asia: Geological Society of America Bulletin, v. 132, p. 2529–2552, https://doi.org/10.1130/B35353.1.
- Li, S., Suo, Y., Li, X., Zhou, J., Santosh, M., Wang, P., Guo, L., Yu, S., Lan, H., Dai, L., Zhou, Z., Cao, X., Zhu, J., Liu, B., Jang, S., Wang, G., and Zhang, G., 2019, Mesozoic tectono-magmatic response in the East Asian ocean-continent connection zone to subduction of the paleo-Pacific Plate: Earth-Science Reviews, v. 192, p. 91–137, https:// doi.org/10.1016/j.earscirev.2019.03.003.
- Liu, T., Zheng, M., and Guo, Z., 1998, Initiation and evolution of the Asian monsoon system timely coupled with the ice-sheet growth and the tectonic movements in Asia: Quaternary Sciences, v. 18, p. 194-204.
- Ma, J., 2020, Sedimentary basin analysis of the Cretaceous ancient desert in the Ordos Basin [Ph.D. thesis]: Beijing, China, China University of Geosciences (Beijing), 73 p.
- Meng, Z., 1994, Magnetostratigraphy of Lower Cretaceous (Hekou Group) near Lanzhou, Gansu: Diqiu Wulixue Bao, v. 37, p. 342–347.
- Miall, A.D., 2006, The Geology of Fluvial Deposits: Sedimentary Facies, Basin Analysis and Petroleum Geology: Berlin, Springer-Verlag, 582 p., https://doi.org/10.1007/978-3-662-03237-4.
- Morin, J., Jolivet, M., Robin, C., Heilbronn, G., Barrier, L., Bourquin, S., and Jia, Y., 2018, Jurassic paleogeography of the Tian Shan: An evolution driven by far-field tectonics and climate: Earth-Science Reviews, v. 187, p. 286–313, https://doi.org/10.1016/j.earscirev.2018 .10.007.
- Murphy, M., Yin, A., Harrison, T., Dürr, S., Chen, Z., Ryerson, F., Kidd, W., Wang, X., and Zhou, X., 1997, Did the Indo-Asian collision alone create the Tibetan Plateau?: Geology, v. 25, p. 719–722, https://doi.org/10.1130/0091-7613(1997)025<0719:DTIACA>2.3.CO:2.
- Nemec, W., and Steel, R.J., 1984, Alluvial and coastal conglomerates their significant features, in Koster, E.H., and Steel, R.J., eds, Sedimentology of Gravels and Conglomerates: Canadian Society of Petroleum Geologists Memoir 10, p. 1–31.
- Pye, K., and Tsolar, H., 2009, Aeolian Sand and Sand Dunes: Berlin, Springer-Verlag, 458 p., https://doi.org/10.1007/978-3-540-85910-9.
- Qian, G., Dong, Z., Luo, W., Zhang, Z., Xiao, S., and Zhao, A., 2011, Grain size characteristics and spatial variation of surface sediments in the Badain Jaran desert: Journal of Desert Research, v. 31, p. 1357–1364.
- Qiao, D., Peng, N., Kuang, H., Liu, Y., Liu, Y., Cui, L., and Wang, Y., 2022, Changes in prevailing surface-paleowinds reveal the atmospheric circulation transition during Early Cretaceous in North China: Palaeogeography, Palaeoclimatology, Palaeoecology, v. 586, https://doi.org /10.1016/j.palaeo.2021.110784.
- Qin, Y., Liu, C., Yang, L., Peng, H., and Jiao, X., 2022, Detrital-zircon geochronology of Jurassic-Cretaceous strata in the Turpan-Hami Basin: Implication for the Late Mesozoic tectonic evolution of eastern Tien Shan: Minerals (Basel), v. 12, https://doi.org/10.3390 /min12080926.
- Quade, J., Breecker, D.O., Daëron, M., and Eiler, J., 2011, The paleoaltimetry of Tibet: An isotopic perspective: American Journal of Science, v. 311, no. 2, p. 77–115, https://doi.org/10.2475/02.2011.01.
- Reis, A.D., Scherer, C.M.S., Amarante, F.B., Rossetti, M.M.M., Kifumbi, C., Souza, E.G., Ferronatto, J.P.F., and Owen, A., 2019, Sedimentology of the proximal portion of a large-scale, Upper Jurassic fluvial-aeolian system in Paraná Basin, southwestern Gondwana: Journal of South American Earth Sciences, v. 95, https://doi .org/10.1016/j.jsames.2019.102248.
- Rodríguez-López, J.P., and Wu, C., 2020, Recurrent deformations of aeolian desert dunes in the cretaceous of the South China Block: Trigger mechanisms variability and implications for aeolian reservoirs: Marine and Petroleum Geology, v. 119, https://doi.org/10.1016/j.marpetgeo.2020.104483.
- Rodríguez-López, J.P., Meléndez, N., De Boer, P.L., and Soria, A.R., 2006, Windblown desert sands in coeval shallow marine deposits: A key for the recognition of

- coastal ergs in the mid-Cretaceous Iberian Basin, Spain: Terra Nova, v. 18, p. 314–320, https://doi.org/10.1111/j.1365-3121.2006.00695.x.
- Rodríguez-López, J.P., Meléndez, N., De Boer, P.L., and Soria, A.R., 2008, Aeolian sand sea development along the mid-Cretaceous western Tethyan margin (Spain): Erg sedimentology and paleoclimate implications: Sedimentology, v. 55, p. 1253–1292, https://doi.org/10.1111/j.1365-3091.2007.00945.x.
- Rodríguez-López, J.P., Meléndez, N., De Boer, P.L., and Soria, A.R., 2010, The action of wind and water in a mid-Cretaceous subtropical erg-margin system close to the Variscan Iberian Massif, Spain: Sedimentology, v. 57, p. 1315–1356, https://doi.org/10.1111/j.1365 -3091.2010.01147.x.
- Rodríguez-López, J.P., Liesa, C.L., Dam, J.V., Lafuente, P., Arlegui, L., Ezquerro, L., and De Boer, P.L., 2012, Aeolian construction and alluvial dismantling of a faultbounded intracontinental aeolian dune field (Teruel Basin, Spain); A continental perspective on late Pliocene climate change and variability: Sedimentology, v. 59, p. 1536–1567, https://doi.org/10.1111/j.1365-3091 .2011.01316.x.
- Rodríguez-López, J.P., Meléndez, N., De Boer, P.L., Soria, A.R., and Liesa, C.L., 2013, Spatial variability of multicontrolled aeolian supersurfaces in central-erg and marine-erg-margin systems: Aeolian Research, v. 11, p. 141–154, https://doi.org/10.1016/j.aeolia.2013.07.002.
- Rodríguez-López, J.P., Clemmensen, L.B., Lancaster, N., Mountney, N.P., and Veiga, G.D., 2014, Archean to Recent aeolian sand systems and their sedimentary record: Current understanding and future prospects: Sedimentology, v. 61, p. 1487–1534, https://doi.org/10 .1111/sed.12123.
- Rodríguez-López, J.P., Wu, C., Vishnivetskaya, T.A., Murton, J.B., Tang, W., and Ma, C., 2022, Permafrost in the Cretaceous supergreenhouse: Nature Communications, v. 13, 7946, https://doi.org/10.1038/s41467-022-35676-6.
- Scherer, C.M.S., Lavina, E.L., Dias Filho, D.C., Oliveira, F.M., Bongiolo, D.E., and Aguiar, E.S., 2007, Stratigraphy and facies architecture of the fluvial–aeolian–lacustrine Sergi Formation (Upper Jurassic), Recôncavo Basin, Brazil: Sedimentary Geology, v. 194, p. 169–193, https://doi.org/10.1016/j.sedgeo.2006.06.002.
- Scherer, C.M.S., Goldberg, K., and Bardola, T., 2015, Facies architecture and sequence stratigraphy of an early post-rift fluvial succession, Aptian Barbalha Formation, Araripe Basin, northeastern Brazil: Sedimentary Geology, v. 322, p. 43–62, https://doi.org/10.1016/j.sedgeo.2015.03.010.
- Scotese, C.R., 2016, PALEOMAP PaleoAtlas for GPlates and the PaleoData Plotter Program: PALEOMAP Project, https://www.earthbyte.org/paleomap-paleoatlas-for-gplates/ (accessed June 2022).
- Şengör, A.M.C., Natal'in, B.A., and Burtman, V.S., 1993, Evolution of the Altaid tectonic collage and Palaeozoic crustal growth in Eurasia: Nature, p. 364, v. 299–307, https://doi.org/10.1038/364299a0.
- Sha, J., 2007, Cretaceous trigonioidid (non-marine Bivalvia) assemblages and biostratigraphy in Asia with special remarks on the classification of Trigonioidacea: Journal of Asian Earth Sciences, v. 29, p. 62–83, https://doi.org/10.1016/j.jseaes.2006.01.003.
- Shen, T., Chen, Y., Wang, G., Ji, J., Wang, Y., Zhang, P., Sotiriou, P., Guo, R., and Xu, Z., 2020, Detrital zircon geochronology analysis of the Late Mesozoic deposition in the Turpan-Hami basin: Implications for the uplift history of the Eastern Tian Shan, north-western China: Terra Nova, v. 32, p. 166–178, https://doi.org /10.1111/ter.12445.
- Smith, A.S., Smith, D.G., and Funnell, B.M., 1994, Atlas of Mesozoic and Cenozoic Coastlines: Cambridge, UK, Cambridge University Press, 99 p.
- Tang, H., 2020, Sedimentary characteristics and palaeoclimatic implications of the Cretaceous aeolian Erg System in the northeastern Chuxiong Basin, China [M.S. thesis]: Chengdu, China, Chengdu University of Technology, 86 p.
- Tang, W., Zhang, Z., Li, J., Li, K., Luo, Z., and Chen, Y., 2015, Mesozoic and Cenozoic uplift and exhumation of the Bogda Mountain, NW China: Evidence from apatite

- fission track analysis: Geoscience Frontiers, v. 6, p. 617–625, https://doi.org/10.1016/j.gsf.2014.04.006.
- Tang, Y., Dai, S., Huang, Y., Zhu, Q., Fang, X., Hu, H., Liu, J., Kong, L., Zhao, J., and Liu, X., 2008, The early Cretaceous tectonic uplift of Qilian mountains: Evidence from the sedimentary facies and susceptibility of rocks of the Hekou group, Lanzhou-Minhe basin: Earth Science Frontiers, v. 15, no. 2, p. 261–271.
- Todd, S.P., 1989, Stream-driven, high-density gravelly traction carpets: Possible deposits in the Trabeg Conglomerate Formation, SW Ireland and some theoretical considerations of their origin: Sedimentology, v. 36, p. 513–530, https://doi.org/10.1111/j.1365-3091.1989.tb02083.x.
- Vincent, S.J., and Allen, M.B., 2001, Sedimentary record of Mesozoic intracontinental deformation in the eastern Junggar Basin, northwest China: Response to orogeny at the Asian margin, in Hendrix, M.S., and Davis, G.A., eds., Paleozoic and Mesozoic Tectonic Evolution of Central Asia: From Continental Assembly to Intracontinental Deformation: Geological Society of America Memoir 194, p. 341–360, https://doi.org/10.1130/0 -8137-1194-0.341.
- Visher, G.S., 1969, Grain size distributions and depositional processes: Journal of Sedimentary Research, v. 39, no. 3, p. 1074–1106, https://doi.org/10.1306/74d71d9d-2b21-11d7-8648000102c1865d.
- Wang, F., Li, Z.J., Sun, X.Y., Zhao, J., Fan, Y.X., Xia, D.S., Ayyamperumal, R., and Li, B.F., 2023, Early Cretaceous (late Barremian–Early Albian) expanding aeolian activity in East Asia: Evidence from the stratigraphic evolution of aeolian deposition in the Baiyin-Jingyuan Basin, northern China: Geological Society of America Bulletin, v. 136, p. 487–512, https://doi.org/10.1130 //B36747.1.
- Wang, H., 2007, Geological Map of Chinese Tianshan and Adjacent Areas: Xi'an, China, Xi'an Center of Geological Survey, Chinese Geological Survey, scale 1:1,000,000.
- Wang, J., 2019, A new specimen of Hamipterus tianshanensis from the Early Cretaceous in Xinjiang, China with depositional environment and Taphonomy analysis [M.S. thesis]: Beijing, China, China University of Geosciences (Beijing), 77 p.
- Wang, X., Kellner, A.W.A., Jiang, S., Wang, Q., Ma, Y., Paidoula, Y., Chen, X., Rodrigues, T., Meng, X., Zhang, J., and Zhou, Z., 2014, Sexually dimorphic tridimensionally preserved pterosaurs and their eggs from China: Current Biology, v. 24, p. 1323–1330, https://doi.org/10.1016/j.cub.2014.04.054.
- Wang, X., Kellner, A.W.A., Jiang, S., Cheng, X., Wang, Q., Ma, Y., Paidoula, Y., Rodrigues, T., Chen, H., Sayao, J.M., Li, N., Zhang, J., Bantim, R.A.M., Meng, X., Zhang, X., Qiu, R., and Zhou, Z., 2017, Egg accumulation with 3D embryos provides insight into the life history of a pterosaur: Science, v. 358, p. 1197–1201, https://doi.org/10.1126/science.aan2329.
- Wang, X., Li, Y., Qiu, R., Jiang, S., Zhang, X., Chen, H., Wang, J., and Cheng, X., 2020, Comparison of the Early Cretaceous pterosaur faunas of China: Earth Science Frontiers, v. 27, no. 6, p. 347–364, https://doi.org/ /10.13745/j.esf.sf.2020.6.19.
- Wang, Z., Li, T., Zhang, J., Liu, Y., and Ma, Z., 2008, The uplifting process of the Bogda Mountain during the Cenozoic and its tectonic implication: Science in China Series D: Earth Sciences, v. 51, p. 579–593, https://doi .org/10.1007/s11430-008-0038-z.
- Williams, M., 2015, Interactions between fluvial and eolian geomorphic systems and processes: Examples from the Sahara and Australia: Catena, v. 134, p. 4–13, https://doi.org/10.1016/j.catena.2014.09.015.
- Windley, B.F., Alexeiev, D., Xiao, W., Kroner, A., and Badarch, G., 2007, Tectonic models for accretion of the Central Asian Orogenic Belt: Journal of the Geological Society, v. 164, p. 31–47, https://doi.org/10.1144/0016-76492006-022.
- Wu, C., and Rodríguez-López, J.P., 2021, Cryospheric processes in Quaternary and Cretaceous hyper-arid plateau desert oases: Sedimentology, v. 68, p. 755–770, https://doi.org/10.1111/sed.12804.
- Wu, C., Liu, C., Yi, H., Xia, G., Zhang, H., Wang, L., Li, G., and Wagreich, M., 2017, Mid-Cretaceous desert

- system in the Simao Basin, southwestern China, and its implications for sea-level change during a greenhouse climate: Palaeogeography, Palaeoclimatology, Palaeoccology, v. 468, p. 529–544, https://doi.org/10.1016/j.palaeo.2016.12.048.
- Wu, C., Rodríguez-López, J.P., Liu, C., Sun, X., Wang, J., Xia, G., and Wagreich, M., 2018, Late Cretaceous climbing erg systems in the western Xinjiang Basin: Palaeoatmosphere dynamics and East Asia margin tectonic forcing on desert expansion and preservation: Marine and Petroleum Geology, v. 93, p. 539–552, https://doi.org/10.1016/j.marpetgeo.2018.03.038.
- Wu, C., Rodríguez-López, J.P., and Santosh, M., 2022, Plateau archives of lithosphere dynamics, cryosphere and paleoclimate: The formation of Cretaceous desert basins in east Asia: Geoscience Frontiers, v. 13, https://doi.org/10.1016/j.gsf.2022.101454.
- Wu, C., Sun, X., Li, G., Huang, L., Jiao, H., Jian, X., Mason, C.C., and Rodríguez–López, J.P., 2023, Cretaceous mountain building processes triggered the aridification and drainage evolution in east Asia: Geological Society of America Bulletin, v. 136, p. 1863–1877, https://doi.org/10.1130/B36763.1.
- Wu, H., Cui, X., Xiong, G., Zhang, Y., and Jiang, X., 2011, Early Cretaceous desert and the reconstruction of palaeowind belts in Gaolan–Baiyin–Jingyuan area, Gansu Province: Dizhi Tongbao, v. 30, p. 1077–1084.
- Xi, D., Tang, Z., Wang, X., Qin, Z., Cao, W., Jiang, T., Wu, B., Li, Y., Zhang, Y., Jiang, W., Kamran, M., Fang, X., and Wan, X., 2020, The Cretaceous Paleogene marine stratigraphic framework that records significant geological events in the western Tarim Basin: Earth Science Frontiers, v. 27, no. 6, p. 165–198, https://doi.org/10.13745/j.esf.sf.2020.6.24.
- Xi, D., Sun, L., Qin, Z., Li, G., Li, G., and Wan, X., 2021, Lithostratigraphic subdivision and correlation of the Cretaceous in China: Dicengxue Zazhi, v. 45, no. 3, p. 375– 401, https://doi.org/10.19839/j.cnki.dexzz.2021.0030.
- Xia, G., Wu, C., Mansour, A., Jin, X., Yi, H., Li, G., Fan, Q., Shi, Z., Murton, J.B., Pei, J., and Rodríguez-López, J.P., 2023, Eocene–Oligocene glaciation on a high central Tibetan Plateau: Geology, v. 51, p. 559–564, https://doi. org/10.1130/G51104.1.
- Xiao, W., Windley, B.F., Allen, M.B., and Han, C., 2013, Paleozoic multiple accretionary and collisional tectonics of the Chinese Tianshan orogenic collage: Gondwana Research, v. 23, p. 1316–1341, https://doi.org/10.1016/j.gr.2012.01.012.
- Xu, H., Liu, Y., Kuang, H., Liu, Y., Peng, N., Dong, C., Xue, P., Xu, J., Cnen, J., and Liu, H., 2013, Sedimentology, palaeogeography and palaeoecology of the Late Jurassic–Early Cretaceous eolian sands in North China: Journal of Palaeogeography, v. 15, p. 11–30, https://doi.org/10.7605/gdlxb.2013.01.002.
- Xu, H., Liu, Y., Kuang, H., and Peng, N., 2019a, Late Jurassic fluvial-eolian deposits from the Tianchihe formation, Ningwu-Jingle basin, Shanxi province, China: Journal of Asian Earth Sciences, v. 174, p. 245–262, https://doi .org/10.1016/j.jseaes.2018.12.012.
- Xu, H., Liu, Y., Kuang, H., Peng, N., Xu, K., and Chen, J., 2019b, Late Jurassic–Early Cretaceous Erg deposits in the Mengyin Basin, western Shandong Province, China: Inferences about the wind regime and paleogeography: Open Journal of Geology, v. 9, p. 700–703, https://doi.org/10.4236/ojg.2019.910079.
- Xu, H., Liu, Y., Kuang, H., Peng, N., and Chen, J., 2021, Diverse preserved dinosaur footprint assemblage from Jurassic Cretaceous transition eolian dune deposits of western Shandong Province, China: Cretaceous Research, v. 121, https://doi.org/10.1016/j.cretres.2020 .104733.
- Yang, Y.T., Guo, Z.X., Song, C.C., Li, X.B., and He, S., 2015, A short-lived but significant Mongol-Okhotsk collisional orogeny in latest Jurassic-earliest Cretaceous: Gondwana Research, v. 28, p. 1096–1116, https://doi .org/10.1016/j.gr.2014.09.010.
- Yi, Z., Liu, Y., and Meert, J.P., 2019, A true polar wander trigger for the Great Jurassic East Asian Aridification: Geology, v. 47, p. 1112–1116, https://doi.org/10.1130 //346641.1.
- Yin, J., Sun, Z., Yang, Z., and Liang, Q., 1999, Cretaceous and early tertiary paleomagnetic results from the

- Lanping basin and its geological implications: Chinese Journal of Geophysics, v. 42, p. 648–659.
- Yu, X., Liu, C., Wang, C., Li, F., and Wang, J., 2020, Eolian deposits of the northern margin of the South China (Jianghan Basin): Reconstruction of the Late Cretaceous East Asian landscape in central China: Marine and Petroleum Geology, v. 117, https://doi.org/10.1016/j .marpetgeo.2020.104390.
- Yu, X., Liu, C., Wang, C., and Wang, J., 2021a, Late Cretaceous aeolian desert system within the Mesozoic fold belt of South China: Palaeoclimatic changes and tectonic forcing of East Asian erg development and preservation: Palaeogeography, Palaeoclimatology, Palaeoecology, v. 567, https://doi.org/10.1016/j.palaeo.2021.110299.
- Yu, X., Wang, C., Bertolini, G., Liu, C., and Wang, J., 2021b, Damp- to dry aeolian system: Sedimentology, climate forcing, and aeolian accumulation in the Late Cretaceous Liyou Basin, South China: Sedimentary Geology, v. 426, https://doi.org/10.1016/j.sedgeo.2021.106030.
- Zhang, D., Wang, G., Pullen, A., Abell, J.T., Ji, J.L., and Shen, T.Y., 2020a, Landscape evolution and development of eolian-modified unconsolidated gravel surfaces and yardangs in the Hami Basin, China: Geomorphology, v. 368, https://doi.org/10.1016/j.geomorph.2020 .107355.
- Zhang, D., Wang, G., Abell, J.T., Pullen, A., Winckler, G., Schaefer, J.M., and Shen, T., 2022, Quantifying late Pleistocene to Holocene erosion rates in the Hami Basin, China: Insights into Pleistocene dust dynamics of an East Asian stony desert: Geophysical Research Letters, v. 49, https://doi.org/10.1029 /2021GL097495.
- Zhang, J., Liu, Y., Flögel, S., Zhang, T., Wang, C., and Fang, X., 2021, Altitude of the East Asian coastal mountains and their influence on Asian climate during early Late Cretaceous: Journal of Geophysical Research: Atmospheres, v. 126, no. 22, https://doi.org/10.1029/2020JD034413.
- Zhang, X., Nie, F., Su, X., Xia, F., Li, M., Yan, Z., Zhang, C., and Feng, Z., 2020b, Relationships between Meso-Cenozoic denudation in the Eastern Tian Shan and uranium mineralization in the Turpan-Hami basin, NW China: Constraints from apatite fission track study: Ore Geology Reviews, v. 127, https://doi.org/10.1016/j.oregeorev.2020.103820.
- Zhang, Z., Wang, H., Guo, Z., and Jiang, D., 2007, What triggers the transition of palaeoenvironmental patterns in China, the Tibetan Plateau uplift or the Paratethys Sea retreat?: Palaeogeography, Palaeoclimatology, Palaeoecology, v. 245, p. 317–331, https://doi.org/10.1016 /j.palaeo.2006.08.003.
- Zheng, C., Wang, J., Li, X., and Zhang, C., 2024, Intermontane erg environment and arid climate indicated from associated eolian and alluvial fan facies during the Late Cretaceous, South China: Journal of Asian Earth Sciences, v. 264, https://doi.org/10.1016/j.jseaes.2024 106044
- Zheng, D., Chang, S., Ramezani, J., Xu, X., Xu, H., Wang, H., Pei, R., Fang, Y., Wang, J., Wang, B., and Zhang, H., 2023, Calibrating the Early Cretaceous Urho Pterosaur Fauna in Junggar Basin and implications for the evolution of the Jehol Biota: Geological Society of America Bulletin, v. 136, p. 765–773, https://doi.org/10.1130 /B36795.1.
- Zheng, H., Wei, C., Tada, R., Clift, P.D., Wang, B., Jourdan, F., Wang, P., and He, M., 2015, Late Oligocene–early Miocene birth of the Taklimakan Desert: Proceedings of the National Academy of Sciences of the United States of America, v. 112, p. 7662–7667, https://doi.org/10.1073/pnas.1424487112.
- Zhu, W., Wan, J., Shu, L., Sun, Y., Guo, J., and Wang, F., 2005, Mesozoic–Cenozoic thermal history of Turpan– Hami Basin: Apatite fission track constraints: Progress in Natural Science, v. 15, p. 331–336, https://doi.org/10 .1080/10020070512331342190.

SCIENCE EDITOR: BRAD SINGER ASSOCIATE EDITOR: ALESSANDRO ZANAZZI

Manuscript Received 11 November 2023 Revised Manuscript Received 26 April 2024 Manuscript Accepted 28 May 2024